Pontificia Universidad Católica del Perú

Escuela de Posgrado

Design and investigations on soft tensegrity structures with magnetic actuation

Tesis para obtener el grado académico de

Magíster en Ingeniería Mecánica que presenta:

Eder Jhoel Avila Mañuico

Asesor PUCP (PUCP): *Prof. Dr.-Ing Jorge Antonio Rodriguez Hernandez*

Co-Asesor de la Universidad no PUCP: *Dr.-Ing Jhohan Harvey Chavez Vega*

Lima, 2023

Informe de Similitud

Yo, Jorge Antonio Rodriguez Hernandez, docente de la Escuela de Posgrado de la Pontificia Universidad Católica del Perú, asesor de la tesis titulada "**Design and investigations on soft tensegrity structures with magnetic actuation**", del autor Eder Jhoel Avila Mañuico, dejo constancia de lo siguiente:

- El mencionado documento tiene un índice de puntuación de similitud de 8%. Así lo consigna el reporte de similitud emitido por el software *Turnitin* el 04/07/2023.
- He revisado con detalle dicho reporte y la Tesis, y no se advierte indicios de plagio.
- Las citas a otros autores y sus respectivas referencias cumplen con las pautas académicas.

Lugar y fecha:
San Miguel 04 de julio de 2023

Apellidos y nombres del asesor: Rodríguez Hernández, Jorge Antonio	
DNI: 06510894	Firma
ORCID: https://orcid.org/0000-0002-5161-7196	*J Rodrig*

Resumen

Las estructuras de tensegridad suave están compuestas por elementos flexibles de elastómeros, que cumplen las funciones de piezas de tensión y compresión. También es posible tener elementos elastómeros que se vean afectados por fuerzas magnéticas, al añadir partículas ferromagnéticas a su composición. Esto abre la posibilidad de accionar una estructura de tensegridad blanda a través de fuerzas magnéticas que pueden afectar algunas partes de la misma. La presente tesis desarrolló un prototipo de mecanismo para accionar magnéticamente una estructura lineal de tensegridad blanda.

Para lograr este movimiento, en primer lugar, se propuso un movimiento oscilante angular para una estructura de tensegridad lineal, y se estableció la configuración de los elementos de tensión pretensados. A continuación, también se explica en detalle el proceso de fabricación, teniendo en cuenta los cálculos por lotes, las consideraciones del molde y los pasos individuales de la fabricación de elementos de elastómero. Finalmente, se diseñó un mecanismo impulsor para accionar la estructura de tensegridad suave, y también se consideraron los cálculos cinemáticos del mecanismo.
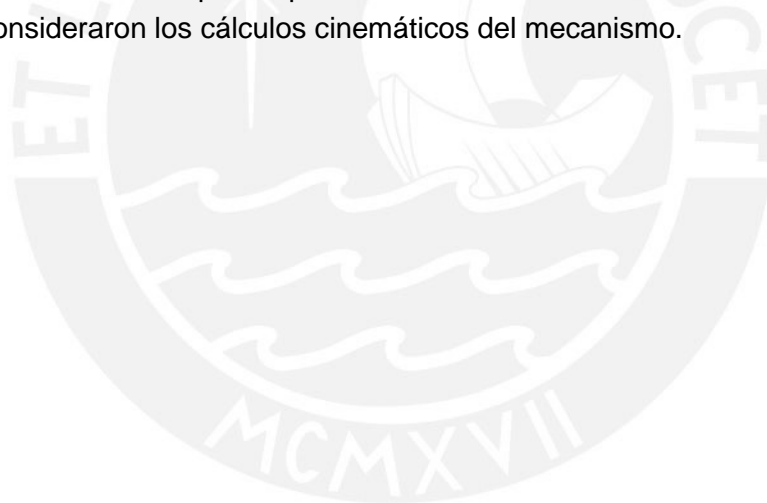
Abstract

Soft tensegrity structures are composed of compliant elastomer elements that fulfill the roles of tension and compression parts. It is also possible to have elastomer elements that are affected by magnetic forces by adding ferromagnetic particles to their composition. This opens up the possibility to actuate a soft tensegrity structure through magnetic forces that can affect some parts of it. The current thesis developed a mechanism prototype to actuate magnetically a linear soft tensegrity structure.
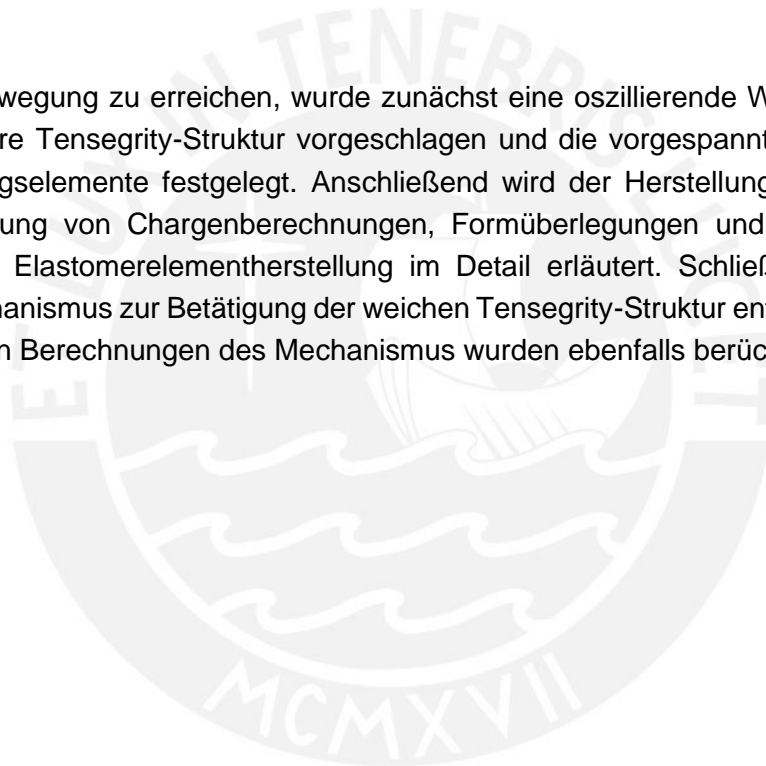
To achieve this actuated movement, first, an angular oscillating movement was proposed for a linear tensegrity structure, and the pre-stressed configuration of tension elements was established. Next, the fabrication process is also explained in detail, considering batch calculations, mold considerations, and the individual steps of the elastomer element fabrications. Finally, a driver mechanism was designed to actuate the soft tensegrity structure, and the kinematic calculations of the mechanism were also considered.
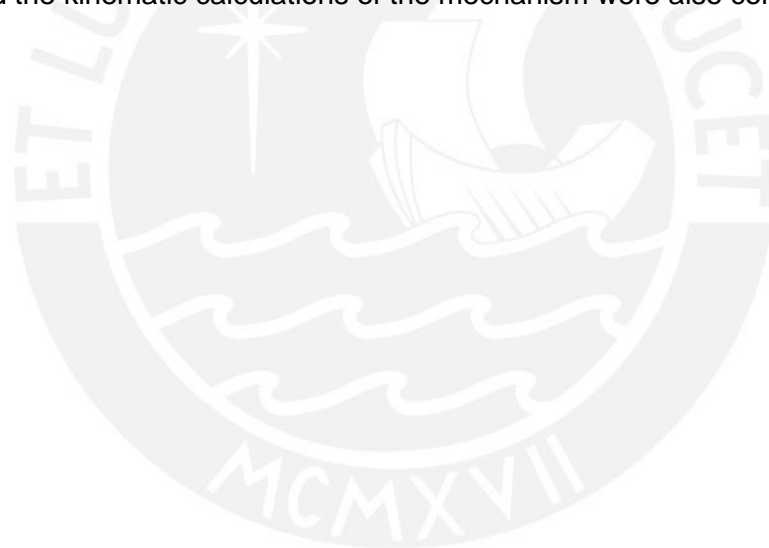
Kurzfassung

Weiche Tensegrity-Strukturen bestehen aus nachgiebigen Elastomerelementen, die die Funktionen von Zug- und Druckteilen erfüllen. Es ist auch möglich, Elastomerelemente zu haben, die durch magnetische Kräfte beeinflusst werden, indem man ferromagnetische Partikel zu ihrer Zusammensetzung hinzufügt. Dies eröffnet die Möglichkeit, eine weiche Tensegrity-Struktur durch magnetische Kräfte zu betätigen, die auf einige Teile der Struktur wirken können. In der vorliegenden Arbeit wurde ein Prototyp eines Mechanismus entwickelt, der eine lineare weiche Tensegrity-Struktur magnetisch antreibt.

Um diese Bewegung zu erreichen, wurde zunächst eine oszillierende Winkelbewegung für eine lineare Tensegrity-Struktur vorgeschlagen und die vorgespannte Konfiguration der Spannungselemente festgelegt. Anschließend wird der Herstellungsprozess unter Berücksichtigung von Chargenberechnungen, Formüberlegungen und den einzelnen Schritten der Elastomerelementherstellung im Detail erläutert. Schließlich wurde ein Antriebsmechanismus zur Betätigung der weichen Tensegrity-Struktur entworfen, und die kinematischen Berechnungen des Mechanismus wurden ebenfalls berücksichtigt.

Acknowledgements

Table of Contents

List of Abbreviations

MRE   :   Magneto-Rheological Elastomers

CIP   :   Carbonyl Iron Powder

STS   :   Soft Tensegrity Structure

DOF   :   Degrees of Freedom

RTV   :   Room Temperature Vulcanization

Figures

Tables

1 Introduction

Tensegrity is a simple yet interesting concept that has surprisingly evolved through the years, from a simple tension-compression disposition to complex applications that go from biological models of the human body to space structures and even robotics.

The first person to apply this concept extensively was the artist, photographer, and sculptor Kenneth Snelson (1927-2016). As such, he threw himself into work that elaborated on these "tension-compression" models held together by their internal tensional elements. This would become a central theme in Snelson's later work (Heartney & Snelson, 2013)

a)   b)

Figure 1-1 a) Early X-Piece Sculpture b) Needle Tower II

(Images from Heartney & Snelson, 2013)

His first sculpture, made in 1948, was the Early X-Piece (fig 1.1 a). It consisted of two wooden, x-shaped pieces held together through metal cables in tension. As he continued to develop his work, his sculptures' complexity and size increased, as seen in his Needle Tower II (fig 1-1 b), a 30-meter tensegrity colossus made in 1969.

Although Snelson was the first to apply the concept of tensegrity consistently, he did not create the terminology for tensile-based structures. That honor belongs to his geometry teacher, Richard Buckminster Fuller, who, in his 1959 patent, used the term "Tensegrity" as a combination of the words "Tensile" and "Integrity".

In this way, Fuller (1959) defined tensegrity as "the discovery of how to progressively reduce the aspect of compression in a structure so that, to a greater extent than has been found possible before, the structure will have the aspect of continuous tension throughout and the compression will be subjugated so that the compression elements become small islands in a sea of tension".
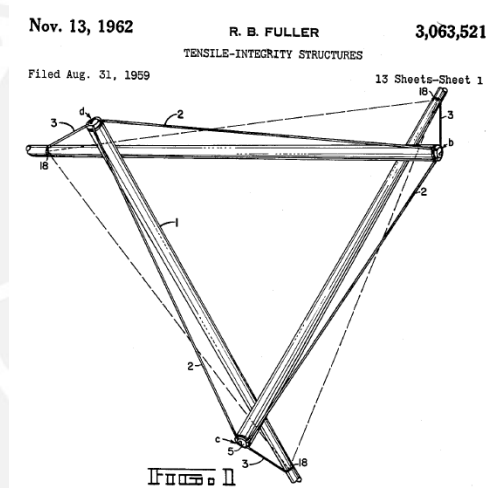
Figure 1-2 R.B. Fuller Tensegrity Patent
(Image from Fuller, 1959)

In his patent for Tensile-Integrity Structures, Fuller envisions possible future applications for the concept of Tensegrity. His ideas went from dome-like structures that could work as a roof for areas as big as a stadium or even a town; to lightweight, collapsible frames that even a rocket could transport.

This last idea was widely applied in aerospace applications, mainly in the solar panels that must be foldable due to the size, volume, and weight limitations of the rockets that will transport them to orbit. As such, the packaging efficiency and the deployment procedure are constantly at odds. One of the solutions applied (Furuya, 1992) is extendible beams that support members of several kinds of substructures on the satellite, like the panels. These beams are often based on deployable tensegrity structures [3].

2
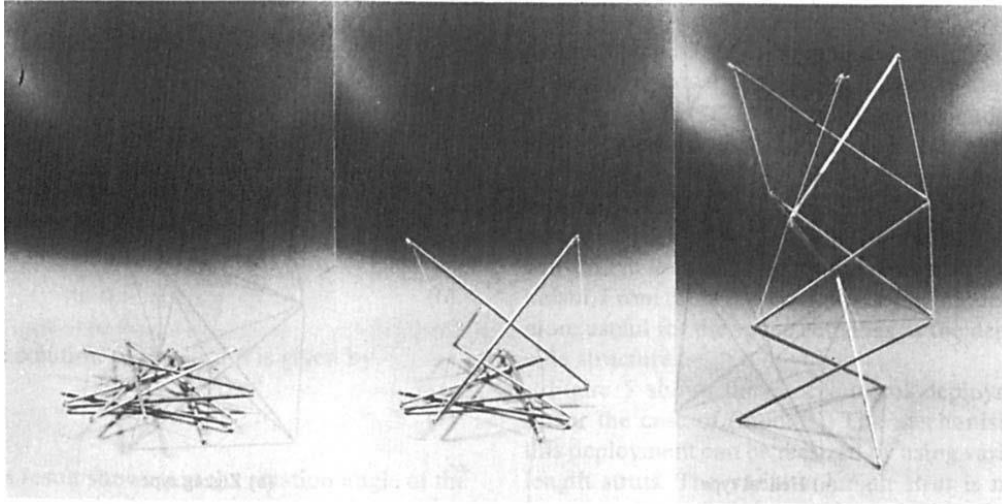
Figure 1-3 Colapsible Tensegrity Structure a) Compressed State b) During Deployment c) Deployed

(Images from Furuya, 1992)

As seen in the previous figure, the collapsible tensegrity structure can be alternated between a compressed state (fig. 1-3 a), in which the structure would be transported, and a fully deployed state (fig 1-3 c), that will keep its stability through tensional elements. These tensional elements will also be part of the deployment process (fig. 1-3 b).

This concept of collapsible tensegrity beams is already applied in several real-world spacecraft. For example, figure 1-4 shows the FAST-mast (Folding Articulated Square Truss) that is currently utilized to support the solar panel arrays of the International Space Station (Belvin et al., 2016).

Figure 1-4 FAST-mast of the International Space Station.

(Image from Belvin et al., 2016)

So far, the concept of tensegrity has gone from an artistic expression of intricate sculptures to stable structures with important real-life uses, such as structural elements in satellites and space stations. However, these tensegrity structures lacked the versatility of movement, a deficiency not present in "Biotensegrity" structures.

The association of the tensegrity architecture to biological organisms, or biotensegrity, began with studying the human spine in the decade of 1970. While it was modeled as a column, the human spine didn't function this way since it can bend in a limited range (Swanson, 2013). Therefore, it was conceptualized through the tensegrity model, similarly to the collapsible beams of the ISS. However, the spine can move while the beams maintain a rigid geometry once deployed. This movement is possible due to the elastic joints the spine is composed of, that work as the tensional elements. Therefore, considering elastic tensional elements, either of variable (muscles) or defined (ligaments) geometry, the whole body can be modeled (Levin, 1982) as a tensegrity structure, with bones working as compression elements. This configures a tensegrity structure capable of either multiple fixed positions and even continuous movement.

The configuration of elements with variable geometry in a tensegrity structure can create multiple fixed positions, also called states of self-equilibrium. These multistable tensegrity structures (Sumi et al., 2017) can have distinguished mechanical properties and shape changes in different equilibrium configurations. Thus, having potential robotic applications, such as the gripper shown in figure 1-5.

Figure 1-5 Gripper application of a tensegrity structure
(Images from Sumi et al., 2017)

Also, continuous movement can be achieved by applying alternating equilibrium states through tensegrity structures. As shown in figure 1-6 a worm-like displacement movement is achieved (Böhm et al., 2021) by alternating equilibrium states of three tensegrity structures linked in a modular way. The actuation is done through a tensioned rope that connects the central nodes of each tensegrity structure module, opening or closing them as required.
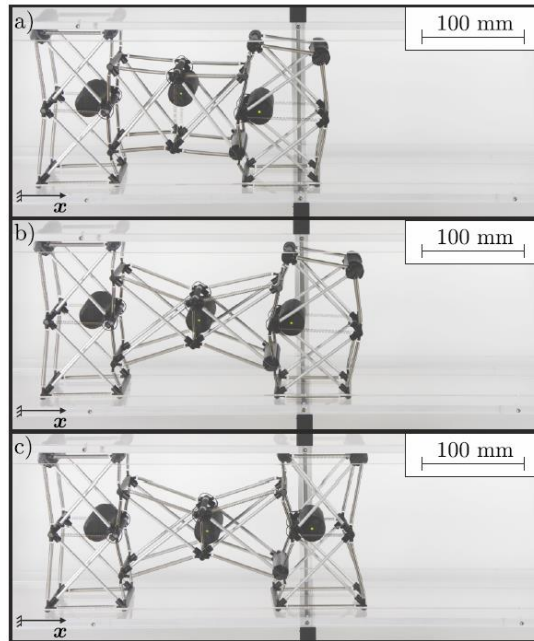
Figure 1-6 Modular Tensegrity Structure in a worm-like displacement
(Images from Böhm et al., 2021)

As seen in the last two examples, the succession of the different equilibrium states is critical to achieving movement in the different robotic applications of tensegrity structures. So far, the structures involved had a rigid nature with several configuration changes, such as pre-stressed tensional elements or geometry changing parts.

1.1 Motivation of study

A new topic in the study of tensegrity is the applications of soft tensegrity structures (STS). This type of structure comprises compliant elements for the tension and compression parts. Because of their mechanical properties, such as a highly elastic behavior, elastomers are suitable materials for soft tensegrity structures. In addition, elastomers also can acquire magnetic properties by including ferromagnetic particles in their composition.

The mentioned characteristics open the possibility of controlling a soft tensegrity structure through magnetic actuation. Since magnetic forces don't require direct contact to be transmitted, this thesis will explore the potential to actuate a soft tensegrity structure to achieve a proposed movement through a barrier that prevents direct contact between the driver and driven elements.

1.2   Objectives of the thesis

The current work focuses on the design, fabrication and designation of actuation mode for soft tensegrity structures based on elastomeric compounds. For this purpose, elastomers with great hardness (Shore hardness A: 30-70) and stiffness are used for the compression members, for which the deformations must be minimized. In contrast for the tension members, highly compliant elastomers (Shore hardness: Scale 00) are used to enable greater deformations.

Main tasks for this thesis are:

- Design and fabrication of compression and tension members of tensegrity structures based on elastomeric compounds
- Design of the actuation mechanism
- Detailed fabrication guideline of the constructed tensegrity structures

1.3   State of the art

In this section, some previous works that were considered in the conception of this thesis thema will be presented. The topics that are considered as crucial for this state of the art are the theory and investigations surrounding Tensegrity Structures, the inner workings of Magneto-Sensible Elastomers (MSE), and the mechanical properties of elastomers.

1.3.1   Tensegrity structures

Tensegrity Structures are arrangements usually composed by elements that are linked by tensional forces, usually a pre-tensed element like a rope, a cable or a spring. Among the different possibilities, a recently discussed topic is the use of mechanically pre-stressed compliant tensegrity structures in soft robotic applications. These compliant structures have multiple states of equilibrium due to their inherent stiffness and shape changing ability. Such characteristics come from the non-linear hyperelastic behavior of the elastomer materials the structure elements are made of.

Below are presented some previous works focused on the possibilities of Tensegrity Structures that contain non-linear hyperelastic elastomer components.

- "Influence of Elastomeric Tensioned Members on the Characteristics of Compliant Tensegrity Structures in Soft Robotic Applications" (Chávez et al., 2020)

In this paper, some aspects on the potential use of elastomeric structure are analysed and compared to the behaviour of a similar tensegrity structure of linear elastic tensioned members. The work is based on a two compressed, 6 tensioned elements, shown in figure 1-7. The members j=1, 2 are the compressed members, while the j=3,4,5,6 elements are the tensioned members.
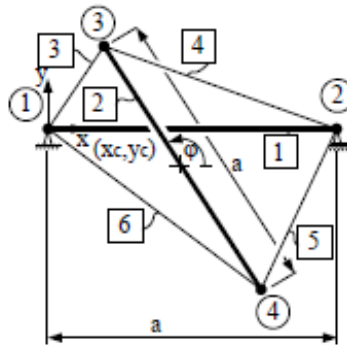
Figure 1-7 Topology of the considered two-dimensional tensegrity structure.

(Image from Chávez et al., 2020)

The most interesting aspect of this work regarding the present project is the analisys of the strain that a non-linear tensegrity structure can achieve, in comparison to a conventional linear structure. While in the case of linear elastic springs, the maximum permited elongation is limited by the yield strength of the material; in the case of elastomers as tensional elements, the strain (formula) is well beyond 100%. In this paper, the maximum strain of the soft tensegrity structure is shown through the working space the selected mechanism can achieve. In this case, it can reach values up to 300% (fig 1-8), far beyond the possibility of most springs.
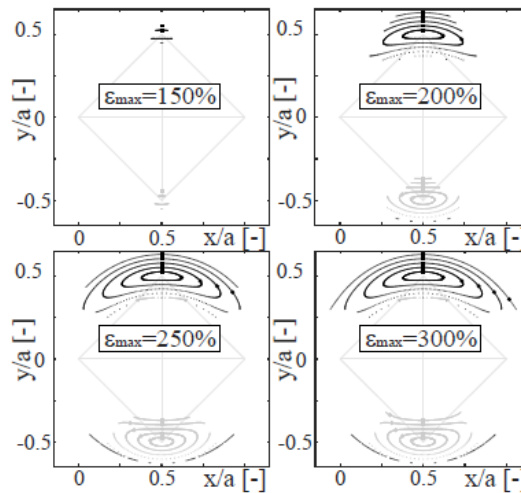
Figure 1-8 Permited working space for various configurations.

(Images from Chávez et al., 2020)

Another characteristic of the elastomer tensegrity strucutures that must be recognized is the hysteresis. In the case of elastomer tension elements, a residual tension force depends on the load history of said element and cannot be neglected. An example of this is displayed in figure 1-9, in which the state 1 is the initial no-load state. The tensegrity structure is the loaded, as shown in the state 2. After the load is relased, the resulting

configuration is different than the intial state 1, due to hysteresis. Hence, the structure only reaches state 3. This aspect of the elastomer behavior must be considered in any future tensegrity application.
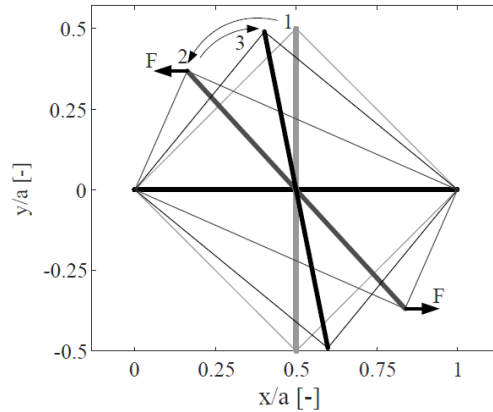
Figure 1-9 Compliant Tensegrity Structure under Hysteresis.

(Image from Chávez et al., 2020)

- "Investigation of a Multistable Tensegrity Robot applied as a Tilting Locomotion System" (Schorr et al., 2020).

In this work, the author uses a tensegrity structure composed of elastomeric tension elements to analyse a hipotetical locomotion movement of the system. The work considers a tensegrity structure as described in figure 1-10, The elements j=1, 2, 3, 4, 5, 6 are the compression elements, the elements j=7, 8 are actuated tension elements, and the elements j= 9, 10 are simple tension elements. The compression elements are made of aluminium rods, considered rigid in this experiment, while the tension elements are elastomers.
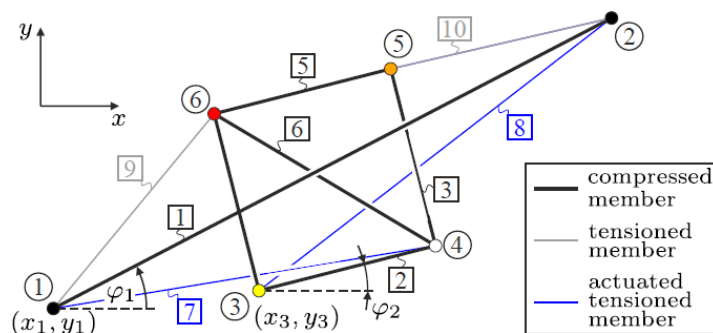
Figure 1-10 Sketch of mobile tensegrity structure.

(Image from Schorr et al., 2020)

The experiment configuration in the real world is distributed along the z axis, and it's purpose is to measure the movement of the joints 3, 4, 5 and 6 (in a circle in figure 1.x). An actuation mechanism varies the effective length of elements j=7, 8, to achieve different

equilibrium states, shown in figure 1-11. The succession of this equilibrium states in the order A->D->C->B->A achieves a theoretical movement, as shown in figure 1-12.
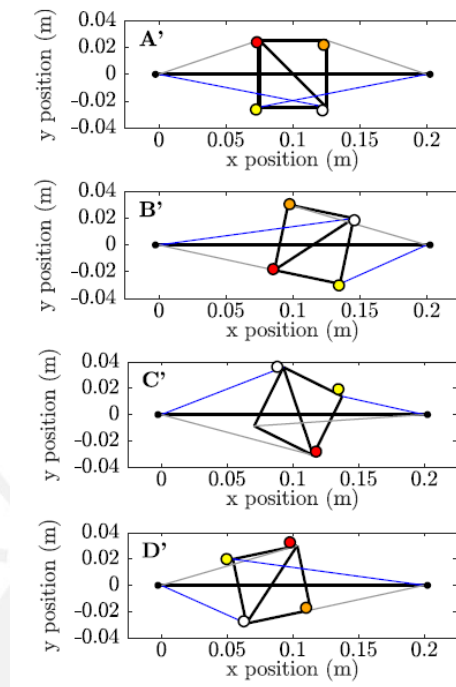
Figure 1-11 Equilibrium states for the tensegrity structures.

(Images from Schorr et al., 2020)
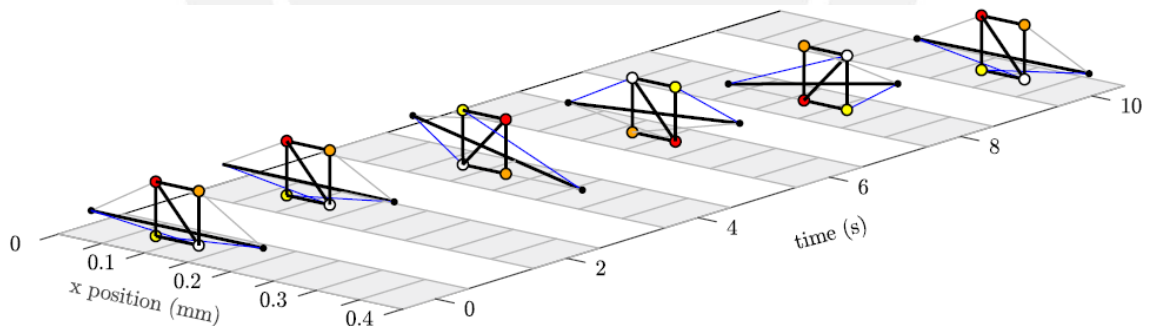
Figure 1-12 Simulation of displacement through tilting movement for actuated compliant tensegrity structure.

(Image from Schorr et al., 2020)

1.3.2 Magneto-rheological elastomers

Currently, some investigations focus on the possibility of elastomers that can be affected by magnetics fields. For this, it is required to add ferrous materials, like carbonyl iron powder (CIP), into the elastomer mix before the vulcanization process. The inclusion of this ferromagnetic powder gives these magneto-rheological elastomers (MREs) some magnetic properties on its own. Some previous works that focus on the properties of MREs and its reaction to magnetic fields are shown bellow.

- "A method to approach constant isotropic permeabilities and demagnetization factors of magneto-rherological elastomers" (Chavez et al., 2021)

This paper focuses on the study of certain magnetic characteristics of magneto-rheological elastomers, analysing samples with different volume concentration of ferromagnetic particles. An MRE is defined as a material that is composed by an elastomer base with dispersed magnetic particles. In the case of this paper, the elastomeric elements are mixed with Carbonyl Iron Powder, a soft magnetic particle.

An interesting characteristic explored in this paper is the magnetic attraction between an MRE and a magnet. For this experiment, cylindrical MRE samples are fabricated, with an elastomerix base of Ecoflex 00-20 and variable volume concentrations of CIP, in a range between 5 to 45%. The samples have a 16 mm diameter and a 12 mm height, and, during the experiment, are encapsulated in a PLA housing, in order to prevent movement. The forces are then measured at different altitudes, with the result displayed in figure 1-13.
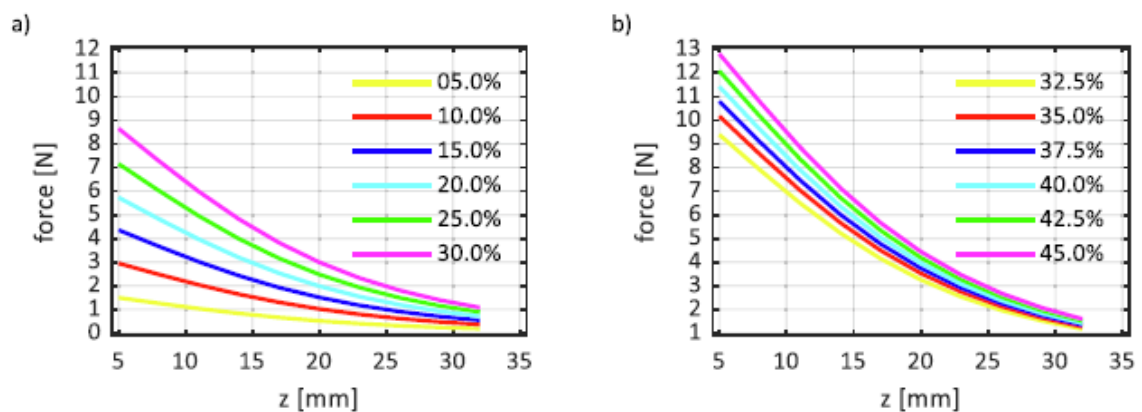
Figure 1-13 Magnetic forces measured for different CIP volumetric concentration a) Range 5-30 %Vol$_{CIP}$ b) Range 32.5-45 %Vol$_{CIP}$.

(Images from Chavez et al., 2021)

From the results, it's possible to realize that a higher volumetric concentration of iron powder in an elastomeric base produces a higher attraction force, when affected by a magnetic field. Also, the results indicate that this attraction force decreases as the distance between the magnet and the MRE increases.

- "Investigations and simulations of magneto elastomer materials (MSE) influenced by static magnetic fields for soft robotics applications" (Lopez, 2019)

In this work, the author studied the accumulative effect on attractive magnetic forces of magneto-elastomer materials, or the capacity to sum the properties measured on small bodies to obtain the properties measured on a larger body [12]. This property was tested by measuring the attractive force of samples with a diameter of 16 mm. The first test

configuration was a unique sample with a height of 12 mm, the second test was done with two samples of 6 mm height, and the last test had a four samples, 3 mm height configuration. The test was done for a 10% and a 20% iron composition.
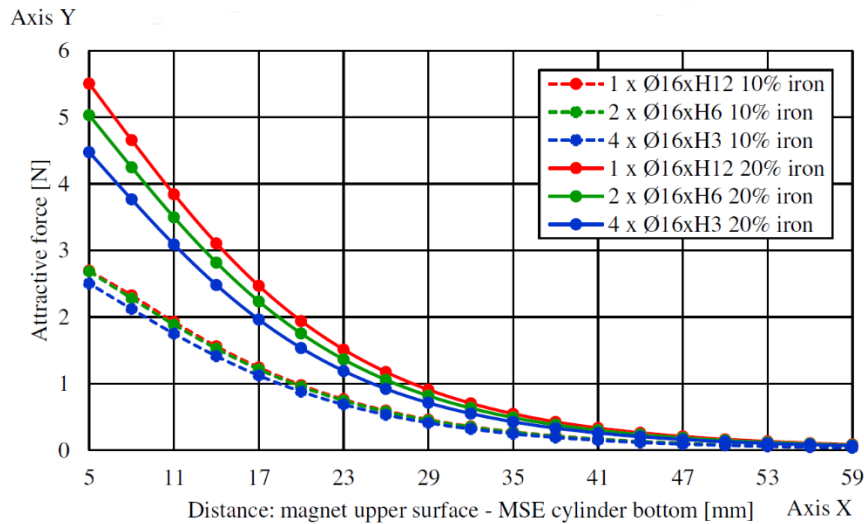
Figure 1-14 Accumulated attractive force, for 10% and 20% vol. iron.

(Image from Lopez, 2021)

While the results in figure 1-14 show a difference between the original and the cumulative forces, due to constructive sources of error, the trend is that the magnetic force of several small samples is similar to the magnetic force of a larger sample, as was initially proposed.

1.3.3 Mechanical properties of elastomers

The articles presented in this section analyzed some of the mechanical properties of elastomers and the variation caused by different ferromagnetic particles' composition content. Comparing the data on tensile strength, it can be noted that different elastomers present similar trends in their properties variation for different compositions.

- "Investigation of the Effect of Carbonyl Iron Micro-Particles on the Mechanical and Rheological Properties of Isotropic and Anisotropic MREs: Constructive Magneto-Mechanical Material Model" (Soria et al., 2019)

This article assesses the addition of carbonyl iron powder to a polydimethylsiloxane (PDMS) elastomer and its influence on several mechanical and rheological properties of the mentioned elastomer. While the paper focuses on both isotropic and anisotropic configurations of the MRE, the current work focuses on the mechanic tensile strength for isotropic elements. The elastomer base used in this work is the Ecoflex 00-10, a compound used in the current thesis work. The tensile test was done according to the
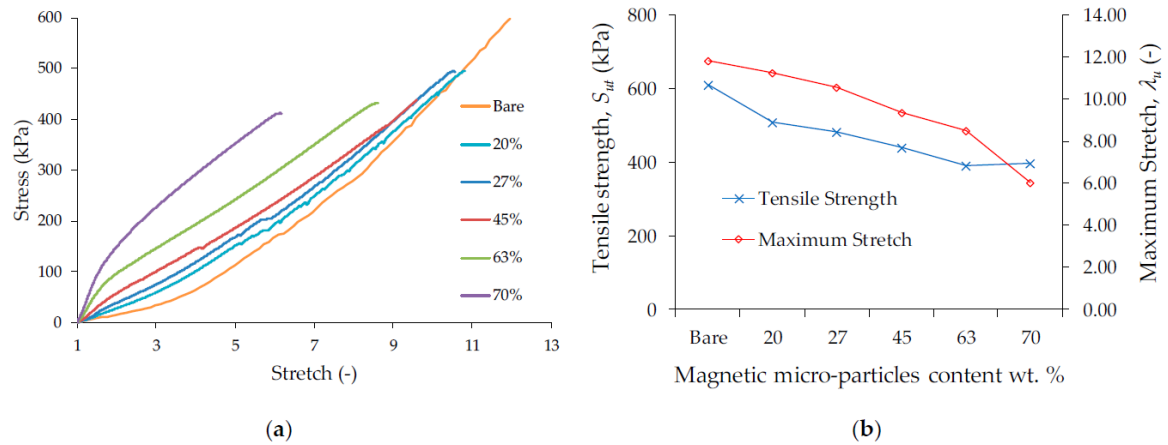
Figure 1-15 a) Tensile test curves for samples with different %wt of CIP b) Tensile strength and maximum stretch for different sample compositions.

(Images from Soria et al., 2019)

Figure 1-15 a) shows the tensile curves for samples of increasing weight percentage of CIP content. The trend shown in this graphic is that, for elastomers with low iron content, the material presents a non-linear stiffening behavior (concave curve). On the other hand, the behavior of elastomers with higher iron content is similar to a non-linear softening (convex curve). Also, when the CIP content increases, the tensile strength, and the maximum stretch tend to diminish, as shown in figure 1-16 b).

- "Investigation of tensile properties of RTV Silicone based Isotropic Magneto-Rheological Elastomers" (Bahktha et al., 2018)

This paper evaluates the tensile properties of a two-part Silicone RTV (Room Temperature Vulcanization) rubber with a different percentage in volume of Carbonyl Iron Powder (compositions between 0% to 30%). The samples were tested according to the standard ASTM D412.

The results of the stress-strain test without any influence of magnetic fields are shown in figure 1-16. The trends displayed in this graphic are similar to those shown in the Ecoflex 00-10 test (Soria et al., 2019). In general, the stiffness of the elastomer increases proportionally to its CIP content, and the tensile stress and the maximum strain decrease. Also, the non-linear behavior for low and high CIP content is similar to the behavior presented in the previous article.
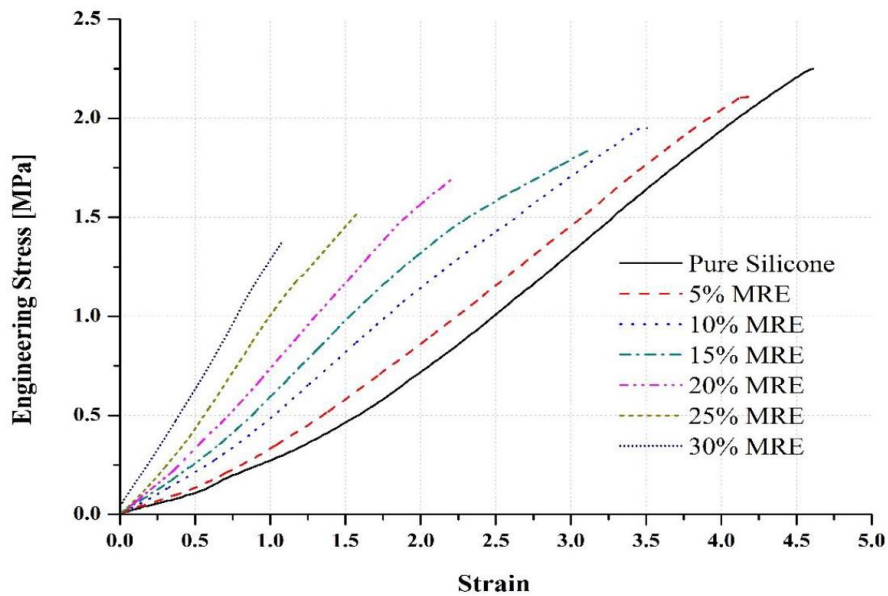
Figure 1-16 Stress vs Strain behavior of different isotropic MREs.

(Image from Bahktha et al., 2018)

2 Soft tensegrity structure

In this chapter, the soft tensegrity structure used in the experiment is described, as well as the proposed movement. Also, there is a description of the actuation method, the materials utilized, the structure elements and the final assembly.

2.1 Concept for the soft tensegrity structure

Inspired on the ideas proposed by the Fachgebiet Mechanik Technik (TU-Ilmenau, 2020a), a multiple unit arrangement of compliant x-members (fig 2-1 a) can be assembled in a grid structure. The idea is to allow this structure to be actuated by an external force, that in this case would be a magnetic actuation. The arrangement would be a structure in a tensegrity state, composed by the x-members as compression elements that would be linked each other by tension elements (in red) in a succession of elementary tensegrity units (fig 2-1 b)

a)   b)
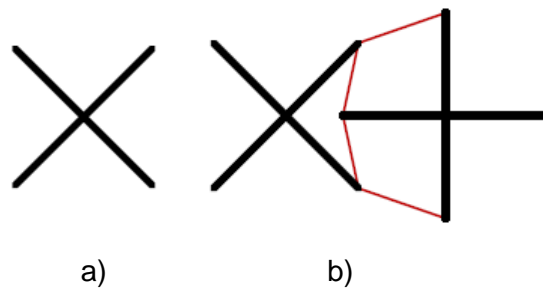
Figure 2-1 a) x-member b) Elementary Tensegrity Unit.

(Image from TU-Ilmenau, 2020a)

For the current project, the tensegrity structure is made up by five compression elements, disposed in a linear arrangement. The proposed movement is an angular oscilation between a straight position and a bended one as seen in the figure 2-2. A certain level of pre-stress must be defined for the arrangement, so it facilitates the actuation of the whole structure.
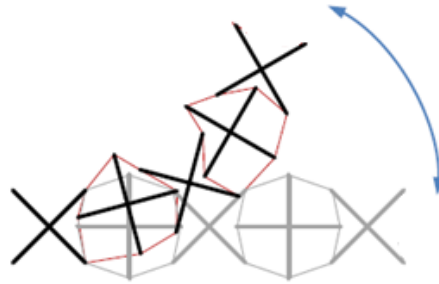
Figure 2-2 Proposed movement.
(Image from TU-Ilmenau, 2020a)

2.2 Magnetic elements

As shown in the section 1.3.2, it is possible for elastomeric compounds to have magnetic properties, through the inclusion of carbonyl iron powder. Because of this, it's possible that an elastomeric soft tensegrity structure can be affected by a magnetic field, if some of its elements has a percentage of iron powder. This opens up the possibility to an external actuation system, based on magnetic interaction between the STS and an actuation mechanism.

The idea for the present thesis project is to actuate certain points of the soft tensegrity structure to achieve the movement proposed before. To show that there is real magnetic actuation, the STS and the magnets must be physically separated, in this case by a 2mm polycarbonate panel. The idea is that an actuation mechanism, that houses and moves certain magnets, can use them to actuate the STS in the proposed angular movement through the polycarbonate panel. The points in which the structure and the mechanism will interact are called magnetic link points.

In the soft tensegrity structure, the tips of the compressed x-shaped members, and the extremes of the tension elements will have magnetic parts. For this, the magnetic sensible elastomers must be capable to be attached to another non-sensible elastomer during the molding process of the latter. This is crucial for material continuity and the transmition of movement, from the actuation mechanism, to the magneto-rheological elastomer parts, to the rest of the STS.

The amount of %vol$_{CIP}$ is an important aspect to consider in the design and fabrication of the magnetic elements, because the strength of the magnetic force is proportional to the amount of iron powder present in the element. However, an increased amount of CIP increases the viscosity of the mixture pre-curing, making the fabrication process harder,

specially during the degassing and molding steps. This is the reason the magnetic elements of the STS will be made with a volumetric concentration of 35% of CIP. This concentration, while high, still allows a viscosity low enough to have a successful fabrication process

2.3 Materials

For this work, there are two types of materials that must be considered. Soft elastomers (shore hardness scale: 00) for the tensional elements, and hard elastomers (shore hardness A: 30-50) for the compression elements.

In the case of the elastomers for the tensional elements, two different sillicones were fabricated, the Ecoflex 00-10 and Ecoflex 00-20. Both of these elements come as two separate compounds (compounds A and B), that are mixed in order to begin the fabrication process. The characteristics relevant for the project experience are listed below in the table 2-1

Table 2-1 Properties of Ecoflex 00-10 and Ecoflex 00-20.

(Table data from Kaupo, 2016)

	Ecoflex 00-10	Ecoflex 00-20
Weight Ratio	1A:1B	1A:1B
Viscosity [mPas]	14000	3000
Specific weight [g/cm^3]	1.04	1.07
Pot Live [min]	30	20
Curing time [hours]	4	4
E-module [N/mm^2]	0.06	0.06

In the STS - actuation mechanism interaction, elements of both compounds were used. However, there was not a diference in the functioning of the system.

In the case of the compression elements, two room-temperature vulcanization (RTV) elastomers were used for fabrication, RTV-27 and RTV-230. While both of this elements have, in paper, excellent properties for the intended use, the fabrication for the RTV-27 presented several problems. The element was hard to degasify, presenting issues better detailed in section 3.5.2 of this document, and had a higher probability to generate air bubbles during the molding process, specially in the union of the RTV mixture with the magnetic terminal previously fabricated. This created a brittle union that could be broken easily. Also, when mixed with CIP, the resulting mixture was more viscous than the RTV-230 counterpart. Because of this, it was very difficult to finish the mixing, degasification and molding processes inside the pot life time gap, that in theory was 60 min [Altropol, 2019a] but in reality the elastomer mix started to cure around 35-40 minutes.

These are the reasons why only the RTV-230 element was used in the experimentation of magnetic actuation on a STS. This element had none of the problems exposed about the RTV-27 element, was easy to fabricate both with and without the incluision of CIP and

almost never presented air bubbles that could be generated during the molding process. The relevant properties of this elastomer compound are presented in the table 2.2 below.

Table 2-2 Properties of Neukasil RTV-230

(Table data from Altropol, 2019b)

	RTV 230	Crosslinker A 149
Mixing ratio	1	1
Density (20^{0}C) [g/cm^3]	1.1	1.1
Viscosity (25^{0}C) [mPa.s]	5000	5000
Pot Life [minutes]	-	40
Curing Time [hours]	-	24
Shore A-hardnes (7d)	-	30
Tensile Strenght [MPA]	-	4.5

2.4 Structure parts

The different elements that compose the soft tensegrity structure are listed below, along with a brief description, dimensions and relevant data for its fabrication.

- Compression Elements: The compression elements are the base of the soft tensegrity structure. These are compliant elements in x-shape, that can bend in accordance to the force applied by the tension elements. For its fabrication, the compression elements required 4 magnetic terminals, that are previously made and located in the compression element mold.

Table 2-3 Fabrication data of Compression Elements

Distance Between Orifices [mm]	60
Height [mm]	4
Volume of Non-Magnetic Part [mm^3}	2750
Elastomer Composition	Neukasil RTV 230 + A 149
Included Elements	Magnetic Terminals (4x)
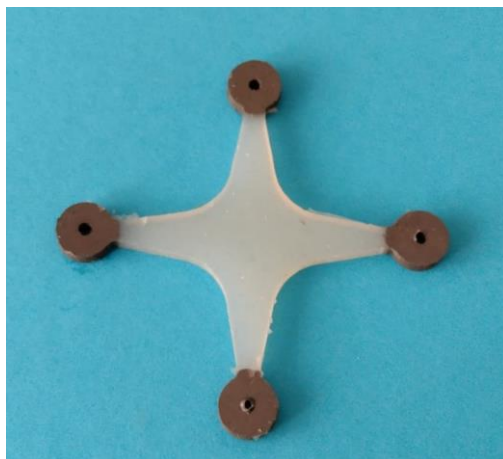
Figure 2-3 Compression Element.

- Magnetic Terminals: This element, made of an RTV elastomer composition mix with CIP, have the task to link the compression elements to the magnets located in the actuation mechanism, through the acrylic barrier that separates it with the STS. The magnetic terminal is shown in figure 2-4 a)

Table 2-4 Fabrication data of magnetic terminals.

Internal Diameter [mm]	2.5
External Diameter [mm]	10
Height [mm]	4
Volume [mm^3]	320
Elastomer Composition	Neukasil RTV 230 + A149 + 35% vol. CIP

- Big Magnetic Ring: This element is a MRE disc that works in the joint as a cap, and as a separator when needed. The big magnetic ring is shown in figure 2-4 b)

Table 2-5 Fabrication data of the big magnetic rings.

Internal Diameter [mm]	2.5
External Diameter [mm]	10
Height [mm]	2
Volume [mm^3]	150
Elastomer Composition	Neukasil RTV 230 + A149 + 35% vol. CIP

- Small Magnetic Ring: These elements, made of an RTV elastomer composition mix with CIP, have the task to link the tension elements to the magnets located in the actuation mechanism, along the other MREs present in the soft tensegrity structure. The small magnetic ring is shown in figure 2-4 c)

Table 2-6 Fabrication data of small magnetic rings.

Internal Diameter [mm]	2.8
External Diameter [mm]	6
Height [mm]	2
Volume [mm^3]	45
Elastomer Composition	Neukasil RTV 230 + A149 + 35% vol. CIP
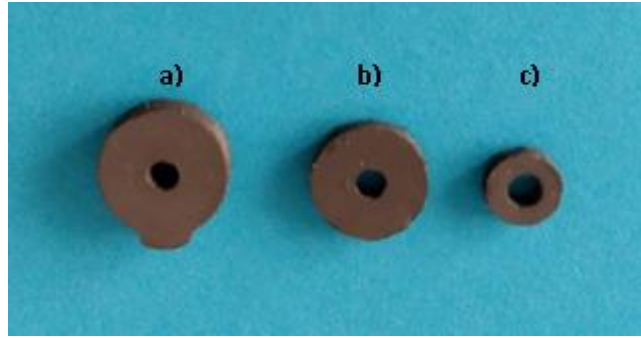
Figure 2-4 Magnetic Elements: a) Magnetic Terminal b) Big Magnetic Ring c) Small Magnetic Ring

- Tension Elements: These elements have a height of 2 mm. and contain 2 small magnetic rings on it's composition. They work as pre-stressed element that link the compression elements. They are made of soft elastomers, either Ecoflex 00-10 or 00-20.

Table 2-7 Volume of tension elements, by length.

Distance between center points [mm]	Volume [mm^3]
12.5	330
15	360
17.5	390

Figure 2-5 Tension Elements in the three diferrent lenghts.

2.5 Structure assembly

As seen in the figure 2-2, the STS will be formed by five compression elements, hold together by sixteen tension elements. This tension elements will have different initial lengths, in order to pre-stress the structure. During the experimentation, it was noted that the best combination of tension elements for the angular movement was the one presented in figure 2-6. The shorter, 12.5mm tension elements would go on the inside. In the middle position, two 15 mm tension elements per elemental tensegrity unit are located, and finally, a 17.5 mm is located in the outer part of the curve.
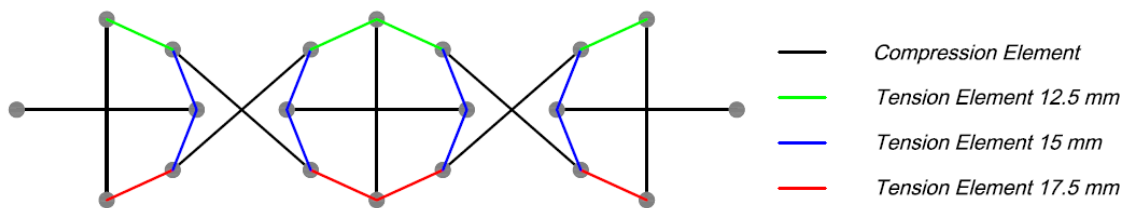
Figure 2-6 Disposition of the Compression and Tension Elements.

This arrangement allows the interior tension elements to help the actuation mechanism in the bending phase of it's movement, while the longer outer tension elements assure that the STS is not stiff enough to not achieve the desired bending movement. Other tension element arrangements were testedm However, they gave some difficulties to the actuation mechanism. For example, replacing the superior 15 mm tension element for its 12.5 mm counterpart, made the structure too stiff, making it harder to the actuation mechanism to go from the bended to the straight position.

In the joints, shown in figure 2-3 as circles, the union of elements will be done through a 3D-printed PLA pin, in a configuration as shown in figure 2-4. Above the plate of the PLA pin goes a tension element, then the compression element, another tension element and finally, the big magnetic ring. In case that an element is not required in a particular joint, a big magnetic ring can replace said element, so the configuration is no altered and the magnetic force in each joint stays the same.
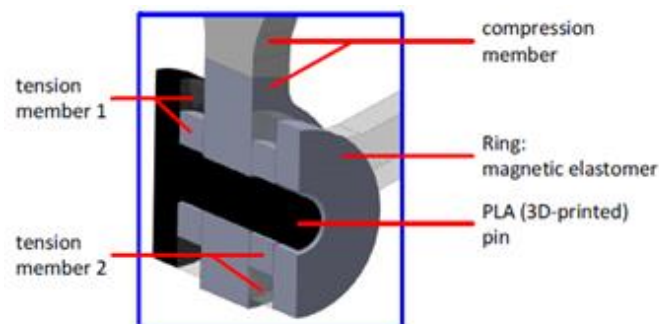
Figure 2-7 Joint configuration.

(Image from TU-Ilmenau, 2020a)

3 Fabrication of soft tensegrity structures

In this section, the details of the fabrication process will be presented, from the equipment used in the fabrication, the different molds used, the calculations required to establish the batch composition, and the fabrication process.

3.1 Fabrication equipment

The main equipment used for the fabrication process is briefly described:

- Beakers: Made of special glass, that prevents chemical reactions with the different materials utilized in the mix, as it serves the function of a container in which the mixing process will be done. The mixing beakers used in the STS fabrication had capacities of 25, 50 and 60 ml.
- Mixing Rods: These are metal rods that serve multiple purposes on the fabrication process. The bigger rod shown in figure 3-1 is used for the mixing of the elastomer compounds, while the middle rod can be used for dosification. The smaller metal rod is used for de-molding the elastomer elements after the curing process is finished.

Figure 3-1 Mixing rods available in the laboratory.

- Laboratory Scale: Highly sensible laboratory equipment, it weights up to an error of 0.001g. Due to its sensitivity, requires cleaning before and after use. Static around it can alter the scale's readings, so this factor must be taken into consideration before
- Extraction Chamber: A glass chamber, composed by a main body and a lid. The lid houses the extraction nozzle and valve, that connects to the void pump. The main body houses a support plate, over which the beaker with elastomer mix is located, and also an intake nozzle and valve, to allow pressurization once the degassing procedure is over.
- Void Pump: A pump that creates a vacuum in the extraction chamber, reaching negative pressures up to -1000 mbar. The vacuum created by the void pump forces the air bubbles inside the elastomer mixture to expand due to the de-

pressurization in the chamber until the bubble bursts, leaving a homogeneous elastomer mixture.
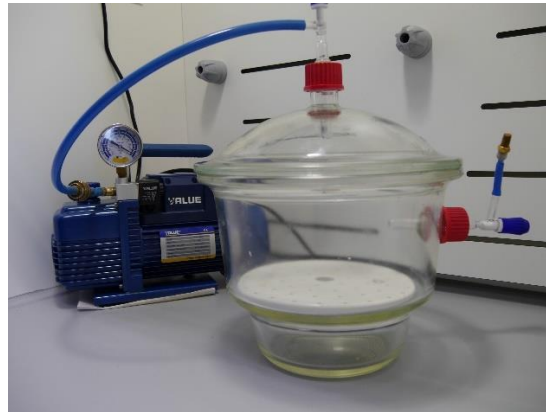
Figure 3-2 Void Pump and Extraction Chamber Configuration.

3.2 Molds

The molds used for the designed STS are made of PLA through a 3D-Printing process. This allows high detail and versatility in the shapes of the elements that can be molded. The disadvantage of PLA molds is that, due to the 3D-printing process, it has internal pores that make them impossible to use in a degasification process. This is the reason why the mix is degasified before the molding.

The molds used in the fabrication of the STS for this work are detailed in the table below. The total volume of a mold is a relevant value to know for the calculation of the batch composition.

Table 3-1 Different Molds and Volume per Batch.

Mold	Element	Volume per Unit [mm³]	Number of Units	Total Volume [mm³]
1	Magnetic Terminal	320	16	5120
2	Compression Element	2750	1	2750
3	Small Magnetic Ring	45	49	2205
4	Big Magnetic Ring	150	16	2400
5	Tension Element - 12.5 mm	330	4	1320
6	Tension Element - 15 mm	360	4	1440
7	Tension Element - 17.5 mm	390	4	1560

3.3 Batch composition

The batch composition states the amount of each component of the mix per batch fabricated. To measure it, the composition is calculated to the weight of the different mixed components. The batch material requirement depends on the number and characteristics of the molds that will be prepared and is stated in volumetric units [mm³]. Because of this, calculations are needed to set the right composition in weight.

The Batch Volume is calculated as the summatory of the mass of the elastomer compounds divided by their density. The density of elastomer compounds is stated in the data sheets of all elastomer mixes. The volume of CIP is also added to this expression (3.1), as a percentage of the required volume for the batch.

$$V_B = \frac{m_{C1}}{\rho_{C1}} + \frac{m_{C2}}{\rho_{C2}} + \%Vol_{CIP} \cdot V_B \quad (3.1)$$

The elastomer mixes are defined by the weight ratio of their components. This information is defined in the data sheets of the elastomer producer, and it's expressed in a ratio formula, as shown in expression (3.2). In this expression, the weight ratio between the masses of Component 1 and Component 2 is a:b. It means that per "a" grams of component 1, there must be "b" grams of component 2.

$$m_{C1} : m_{C2} \Rightarrow a : b \quad (3.2)$$

$$m_{C1} = \frac{a}{b} m_{C2} \quad (3.3)$$

Considering the ratio between the mass of components 1 and 2, it is possible to know the value of one of the masses by knowing the other (3.3). Replacing this relation in equation (3.1), it is possible to calculate the mass of component 2. All the terms in equation (3.4) are known, and in the case of elastomer mixes without any CIP percentage, this value is equated to zero. To calculate the mass of CIP required, the volume it represents in the mix is multiplied by the density of the CIP (7.87 g/mm³), as shown in the expression (3.5)

$$m_{C2} = \frac{V_B(1 - \%Vol_{CIP})}{\left(\frac{a}{b \cdot \rho_{C1}} + \frac{1}{\rho_{C2}}\right)} \quad (3.4)$$

$$m_{CIP} = \%Vol_{CIP} \cdot V_B \cdot \rho_{CIP} \quad (3.5)$$

While the masses so far calculated consider a theory required batch volume, the actual fabrication process requires additional material due to material waste. The reason for this waste is mainly the amount of material that stays stuck in the mixing beakers and extra material required by the molding process to minimize the possibility of air bubbles generated in this fabrication step.

The extra material required is around 2 to 4 grams of the mixture, depending on the beaker. The beaker selection also considers the original weight of the elastomeric compounds of the batch (it does not consider the weight of the CIP). For bigger batches, a bigger beaker is required to allow a better mix movement and a reduced possibility of bubble overflowing the recipient. The downside of this is an increase in material waste attached to the beaker's walls. Therefore, a balance between benefits and downsides is required for beaker selection. The recommended additional material also considers the extra material required by the molding process.

Table 3-2 Recommendations for Additional Material.

Original Batch Elastomer Weight [g]	Recommended Beaker [ml]	Recommended additional Material [g]
2-3.5	25	2
3.5-4.5	50	2.5-3
4.5 or more	60	4-5

To calculate the new batch composition, weight relations between the calculated mass values of the beakers, as the original batch is required (3.6). To ease the calculations, these relations are expressed as multiples of the value of m_{C1}. Then the mass of the new batch composition is evaluated as a summation of multiples of the mass of C1. (3.7). By solving this equation, the value of m_{C1} is calculated and is now possible to calculate the other mass values through the weight relations (3.6), having the final batch composition defined.

$$m_{C2} = c \cdot m_{C1} \ ; \ m_{CIP} = d \cdot m_{C1} \text{ (3.6)}$$

$$m_B = m'_{C1} + c \cdot m'_{C1} + d \cdot m'_{C1} \text{ (3.7)}$$

3.4 Fabrication process

With the batch composition defined and all the weights of the mixture components calculated, the fabrication process for the elastomer elements of the soft tensegrity structure begins. This process comprises four steps, dosage, mixing and degasification,

molding, and de-molding. In this section, the details of these processes are described, along with some personal observations.

3.4.1 Dosage of elastomer compounds

The elastomer elements fabrication process starts with the dosage of the elastomer components. It is required to have all elements and tools on hand, since the curing of the elastomer mixture begins as soon as both reactive components get together, meaning that there is a limited time from start to molding.

The first step in this process is to grade the zero on the laboratory scale. For this, the scale must be turned on, after being cleaned previously. The selected mixing beaker is then located on top of the scale's plate. When the reading on the scale's screen stabilized, then it's time to press the "TARE" button on the scale, to set a starting point.

The next step in the fabrication procedure is to pour the elastomer components into the mixing vase. There are several considerations to take into account for this process. The first is to do it slowly, so the amount of material poured into the vase does not go over the required weight of the batch composition. There is an acceptable error range of ±0.005 g. on the measured weight of any component. Also, there is the possibility of using the metal palettes to take the components out of their bottles. It allows better control of the pouring process

Another consideration is the order of the components in the pouring process. When dealing with mixtures between a main component and a far less viscous additive (i.e. RTV-27 and A-43), it's better to pour the main component first, because if there is a weighting mistake, the material can be easily extracted. The less viscous additives are also easier to control when poured with the ribbed pallete since it goes down by droplets. Also, when working with mixtures that include iron powder, a way to delay the start of the curing reaction is to pour the first main component, then a layer of iron powder, and then the final elastomer component. It is also important to set a zero level on the scale after finishing the weighting process of each component.

One final consideration to take into account is the static electricity that can be stored in the components' containers. Due to the cleaning of the containers, done with absorbent paper, there is some static in them. This alters the reading of the scale, in the order of even ±0.1 g, a deviation that has a considerable impact on the weight percentages of the components in the mixture. An easy way to solve this issue is to use a teaspoon to hold the element first and pour the component from it, minimizing the static effect over the scale lecture. A teaspoon can hold around 3.5-4 g. of elastomer component.

3.4.2 Mixing and degasification

The mixing process begins when the components are already dosed and on the mixing beaker. For this, the metal rods are used, and by moving them inside the components' mix, a good mixture can be achieved. The movement required for the mixing is usually circular, alternating clockwise and counterclockwise directions. Another significant movement is dragging material from the beaker's outer side to the interior as displayed in figure 3-3. This last movement is especially recommended for batches that include iron powder.
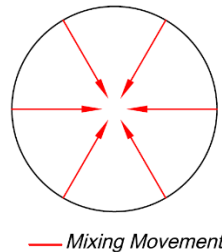
— *Mixing Movement*

Figure 3-3 Metal rod movement to mix CIP.

The mix is considered blended after 3-4 minutes of continuous mixing. While a longer mixing time would assure a perfect blending, it also adds more air into the mixture and reduce the available time for degasification and molding, considering the time limitations of the curing starting time for each component. For iron powder compositions, the homogeneity of color on the surface is also a factor to take into account when evaluating the adequacy of the mixing process.

The mixing process introduces a considerable amount of air bubbles into the mixture, compromising the final material's structural and mechanical properties. For this reason, a degasification process is required. In this project, a void pump is used to drop the pressure of an extraction chamber below atmospheric pressure to eliminate all air bubbles contained in the elastomer mix.

In order to start the degasification process, the mixing beaker is positioned in the extraction chamber below the extraction nozzle. In the case of the iron powder mixtures, due to their high viscosity, it is recommended to set the mixing beaker in an inclined position, as shown in figure 3-4. This inclination is achieved by utilizing a plasticine block that adapts to the mixing vase inclination angle, shape, and size. With the beaker in position, the chamber and all valves are closed and then the void pump is turned on.
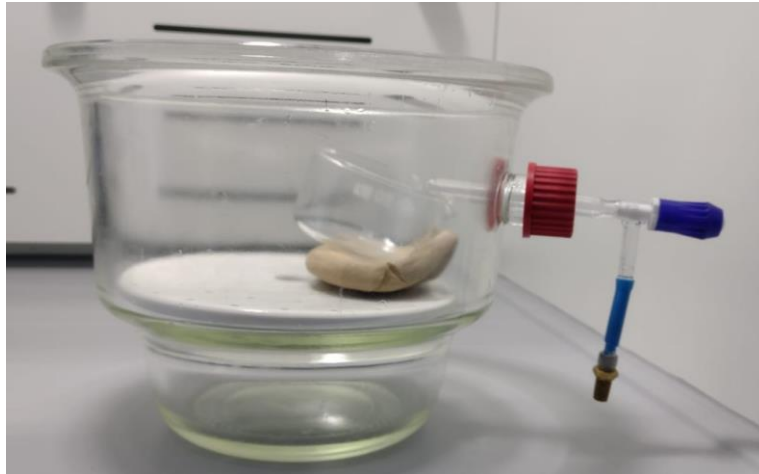
Figure 3-4 Positioning of the inclined mixing beaker bellow the nozzle.

During the degasification process, the mixture forms bubbles on its surface. In some cases, these bubbles can grow beyond the size of the vase, so the extraction valve must be open briefly to avoid the content overflowing the beaker into the extraction chamber.

Also, in higher viscosity mixtures, sometimes there are difficulties for the bubbles to break. There are possible solutions to this issue by handling the extraction nozzle and valve. The first, more straightforward solution is to open the extraction valve violently, so the sudden increase in pressure inside the chamber breaks the air bubbles. If this option does not work, it is possible to rotate the nozzle around $180°$ (figure 3-5), so the opening on it points directly to the mix. Then the extraction valve must be opened slowly until a slight air breeze enters the chamber. The opening is then rotated lightly, so it targets the position of the air bubbles in the mix. The air current will break the bubbles in the area, both because of the sudden pressure variation and the air impact. This process must be done carefully because a strong air current can spill the mixture over the extraction chamber.
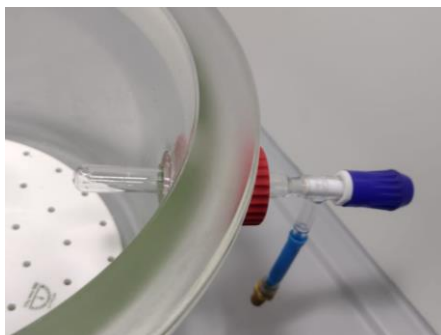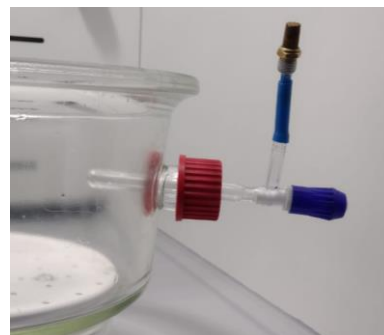
a)   b)

Figure 3-5 Rotation of the input nozzle in the extraction chamber.

3.4.3 Molding

With the mixture degasified, it is crucial to start the molding process as soon as possible. The solidification of elastomer components begins between 10 to 60 minutes after mixed, according to the datasheets of the materials. In reality, the mix solidification can start earlier, affecting the molding process, so speed is essential. Also, fixing the mold on a stable and even surface, like a desk, is recommended. This fixation can be accomplished by attaching a double side tape to the bottom of the mold and the desk's surface. The mold must be fixed at the edge of the desk, so a clamp can be used to press the mold and the polycarbonate plate that will seal the elastomer mix.

An essential task in molding is to avoid air pockets when pouring the mix into the mold, especially in the case of more viscous components, like the iron powder elements. These pockets can be prevented by carefully moving the elastomer stream alongside the mold. However, a wrong stream movement, in conjunction with the viscosity of the elastomer mixture, can increase the probability of air bubbles in the final parts.

In the case of the circular elements, the best way to pour the mix into the mold is to do it with a circular movement (fig 3-6), alternating clockwise and counterclockwise displacements of the stream. It is also important to not complete the circle, to let the flow of the material fill that gap more gradually and naturally. Since these elements come in arrays of many parts, it is recommended to fill a mold for a single piece with up to half of the required material and then continue with the next mold so the mix inside the first mold has time to fill in the gaps. Then is possible to go back to the half-filled molds to finish the pouring of material.
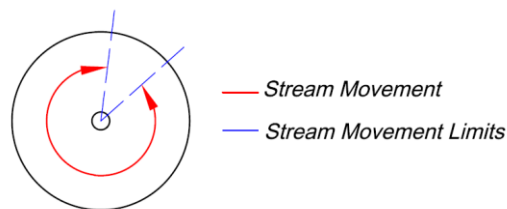
Figure 3-6 Pouring movement of elastomer stream in circular molds.

In the case of the compression elements, it must be noted that before the molding process, the magnetic terminals must be collocated in the extremes of the mold. The tip of the magnetic terminals must have a uniform surface because a rugged surface can prohibit the elastomer mix from distributing correctly and form an air bubble. The best way to pour the elastomer mixture into the mold is to start from the center. This way, the mixture is distributed uniformly in the central part. When the mixture enters the arms of the mold, a slow stream movement can be done in the direction of the element's tips (fig 3-7) without getting close to the magnetic terminal. This restriction allows the mixture to fill that gap more gradually.
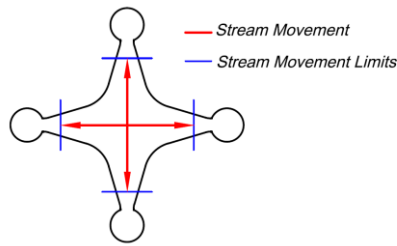
Figure 3-7 Pouring movement of elastomer stream in compression element molds.

The molding of the tension materials is probably the easiest of all the elements of our STS. Moreover, since the materials used for these parts are the less viscous of all the materials used, it's the least probable to form air bubbles in the molding process. Still, to minimize this possibility even more, it's recommended to fill the mold with a movement of the stream alongside the central part of the tension element mold (fig 3-8), avoiding the space in which the magnetic ring must be previously placed.
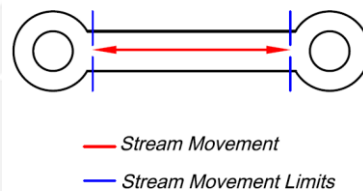
Figure 3-8 Pouring movement of elastomer stream in tension element molds.

After pouring the elastomer mix into the mold is complete, a polycarbonate plate is laid on top of it, sealing the elastomer mixture. This process also has a risk of generating air bubbles. To avoid this problem, it is recommended to fill the mold with some extra material, so there are no air bubbles due to the elastomer not filling the mold. Also, the plate must be dropped inclined, starting in one of the borders of the mold and falling to the other side. It is essential to do this process slowly, so the elastomer mix being pressed has enough time to distribute itself and doesn't form any air bubbles. Keeping the polycarbonate plate in position, a clamp must be located, pressing the mold-plate configuration to the desk. Once the plate is in place, it must not move or be taken off the mold because that could form many bubbles and ruin the molding process. The clamp must be closed and apply pressure on the plate, but excessive force is not recommended. Usually, just one more press on the clamp's handle after the clamp makes contact with the polycarbonate plate will suffice.

3.4.4   De-molding

Depending on the solidification time of each elastomer, the STS elements will take between 4 to 24 hours to solidify. After this solidification time, there are no problems with taking the parts out of the mold. For this, there are some considerations to take into account.

Before trying to take the elastomer parts out of their molds, the excess material between the mold and the acrylic plate must be removed. The big pieces of extra material can be taken out by hand, while some small pieces attached to the main parts can be taken off by rubbing the surface of the mold with absorbent paper. When there is no more material excess, the demolding process can begin.

For the circular elements, a small metal rod can be used to help in the demolding process. The rod can be introduced into the element's side and gently be moved alongside the element's circumference. As it moves, it is also used as a lever, trying to take the circular element out of its mold. It is essential not to use excessive force in this lever movement because it can break the internal pin of the circular mold, thus making such mold useless. It is also important not to harm the lateral surface of the elements while doing the levering.

The compression elements are easier to take out. A similar process as the one for the circular elements can be done for the magnetic terminals. Since the terminals were already curated before the molding of the compression element, it is not attached to the walls of the mold, so it gets out quickly. After one or two terminals are out, the compression element can be removed by pulling it by the terminals. It is crucial to be careful in the pulling process so as not to break the pins of the mold in the part that houses the magnetic terminals because they can also break. While breaking a pin will not make the mold useless, it can affect the subsequent molding processes by allowing material in the center of the magnetic terminals. Although this material can be taken out, it is not desirable.

The tension elements are the easiest ones to take out. Once clean of excess material, the small metal rod is introduced on the side of the central part. From there, it levers the element while trying to reach the bottom of the magnetic ring. By levering this ring, the part quickly gets off the mold. Since this pin is short, the probability of breaking the mold pin in the process is relatively low.

3.5 Other considerations

3.5.1 Elastomer viscosity

The elastomer viscosity is an important characteristic to consider, especially during the molding process. For elastomer mixtures that do not contain CIP, there are not many problems regarding its viscosity, but when the CIP is added to the mix, the molding process becomes more difficult. The mixture's viscosity is increased, so it is more difficult to start pouring it into the molds. To ease this situation, a solution is to degasify the mixture with the beaker in an inclined position to give the flow stream a head start when beginning the molding.

Another problem regarding viscosity is that the elements containing CIP had a shorter time before curing. While the datasheet of the elements indicates a pot-life time when mixed, this time is reduced by the start of the curing process, so the real-time range in which the mixture can be molded effectively is uncertain. When dealing with big elastomer batches (i.e., molds 1, 3, and 4 simultaneously), there is a possibility not to finish the pouring process because the mixture starts curing and does not flow anymore. Another

issue is that the mixture increases its viscosity as time progresses, so the spaces in the mold are more challenging to fill by the normal flow of material. These not filled spaces increase the possibility of having air bubbles in the final element. When the degasification time and difficulty are included, the uncertainty of a correct molding process for elements containing CIP is increased.

3.5.2 Degassing by vibration

The degassing process through vacuum chambers effectively eliminates air bubbles inside an elastomer mix before curing. However, it has disadvantages, like an excessive bubble formation that can overflow the mixing recipient or bubbles that do not break down at the minimum negative pressure the disposable vacuum pump can reach.

A degassing by vibration process was an alternative explored as an additional measure during the degassing process for the RTV 27 elastomer mixture. Vibration is a method used to degasify diverse mixtures, like concrete (Koch et at., 2019) or even molten metal (Puga et al., 2021). Since the number of air bubbles for the RTV 27 mixture was higher than the ones formed after mixing the RTV 230, resulting in an immediate overflow of the mixing recipient, that made complex the application of the additional degassing methods mentioned in section 3.4.2.

To solve these problems, the mixing beaker was initially given minor knocks on the table to introduce some vibration into the mix. The result was a reduced amount of air bubbles in the mixture, no overflow, and a faster vacuum degassing process. While successful, this method is kind of rudimentary. In addition, it has some risks, like the possibility of spilling the content of the beaker or damaging the recipient if the user is not careful. However, this method could be improved.

4 Actuation mechanism

The required movement for the present experiment is an oscillatory angular movement, in a 45º angle range, in the fifth element of the STS, as defined in chapter 2 of the current document. The detail of the movement is shown in figure 4-1.

a   b
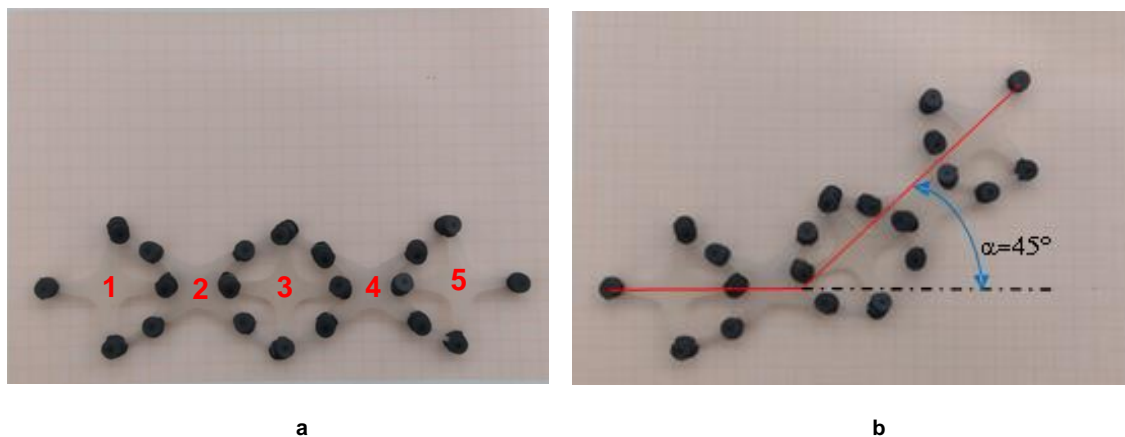
Figure 4-1 STS in (a) straight dead point and (b) bent dead point

In order to achieve this kind of movement in the STS, a magnetic actuation mechanism must be designed. A planar four-bar mechanism (figure 4-2) will be designed based on the required movement. This mechanism can provide an oscillating angular movement in its driven element. In this case, the angle range of the said driven element will be 45^0.
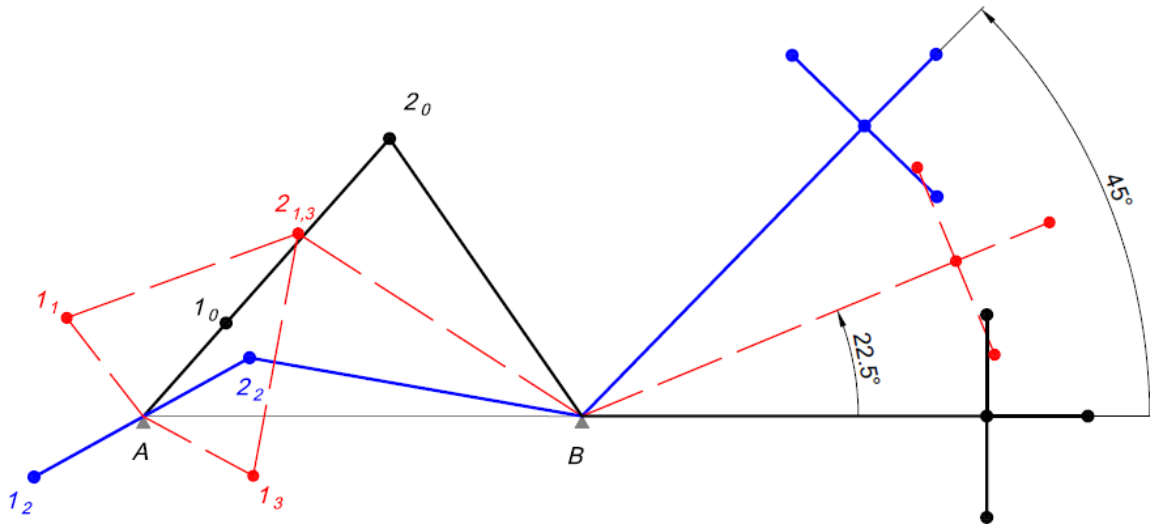
Figure 4-2 Concept of four-bar mechanism, in 3 different positions.

In order to link the mechanism with the STS, magnetic link points must be selected, both for the fixed positions and the mobile points. Figure 4-3 shows the link positions in the STS. The fixed link points are shown in red in the first element in the STS. The fifth element shows the mobile or actuated link points in green.
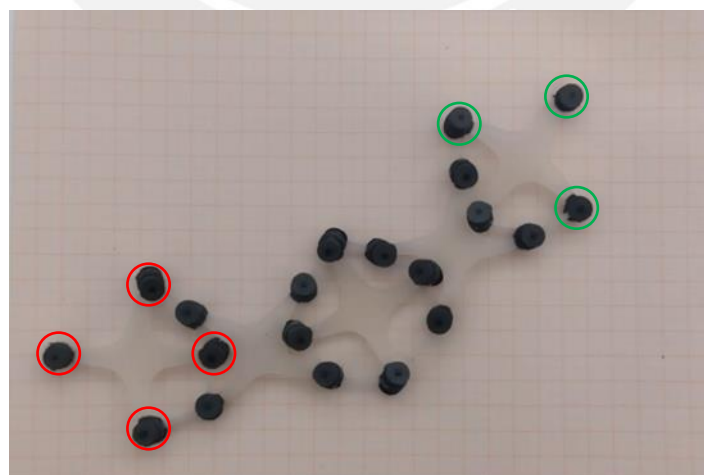
Figure 4-3 Magnetic Link Points in STS.

Considering that space is needed to house the electric motor, which will also work as fixed-point A and space for fixed-point B, the distance between both fixed points will be 130mm. The configuration of the STS and Mechanism can be shown in figure 4-4. It is to be noted that point B is superposed with the STS and in no contact or magnetic link with it.
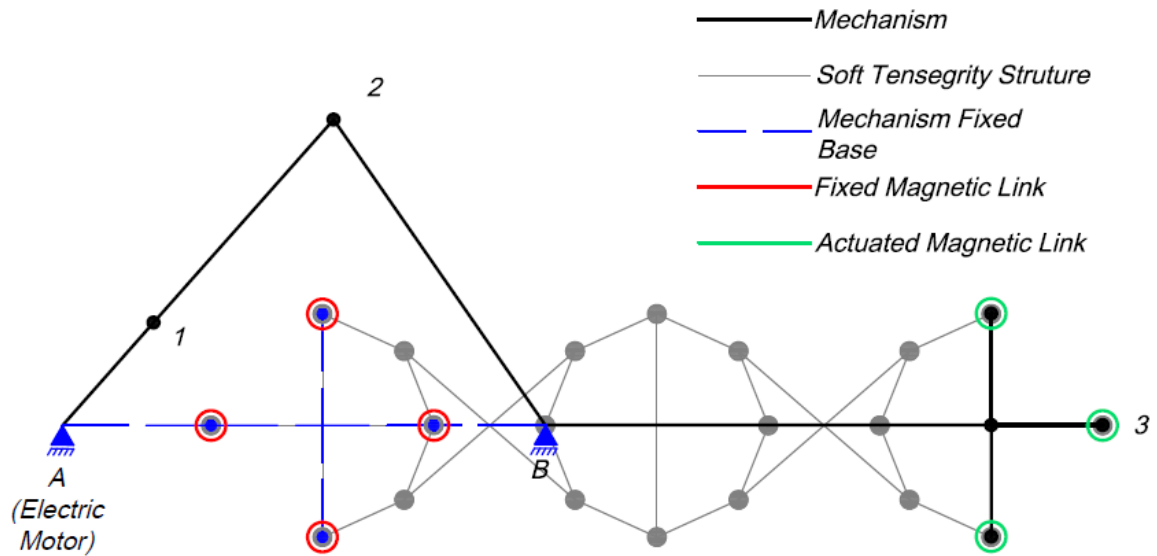
Figure 4-4 Mechanism and Fixed Base over STS.

4.1 Concepts for the actuation mechanism design

The design of the actuation mechanism can be divided into two parts, the synthesis and the dimensioning of the main components of a four-bar mechanism and the kinematic calculations that can be done to determine the behavior of the actuation mechanism.

4.1.1 Mecanism synthesis theory

Given the position at straight and bent dead-points of the required movement, the method utilized will be based on evaluating these dead points, meaning the start and finish position of the driven element of the mechanism.

As shown in figure 4-5, for a four-bar mechanism, positions A and B represent the articulations' position in one of the two dead-point states, while positions A_i and B_i refer to the other. The arc ψ_0 represents the range of movement of the driven element from the first to the second dead-point state, while the angle φ_0 represents the angular displacement of the driver element between dead-point states. To determine the mechanism's dimensions for a distance between given fixed points A_0 and B_0, said mechanism must comply with the requirement of movement transfer, which is the range

ψ_0 of the driven element that a driver element must generate in an φ_0 angular displacement of φ_0. It is important to note that at both dead-point states, the driver and the transmission elements of the mechanism are collinear.
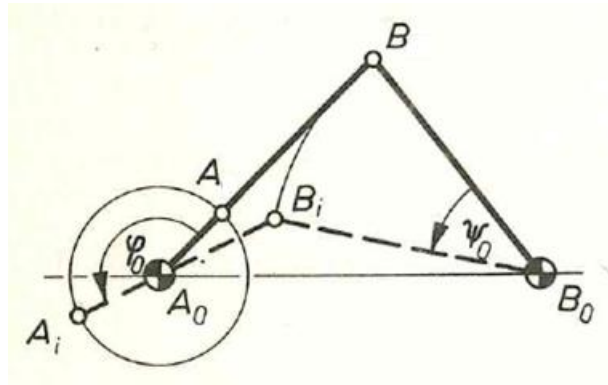
Figure 4-5 Four-bar mechanism in both dead-point states.

(Image from Luck & Modler, 1995)

The graphic method used to design this mechanism is based on the work of Herman Alt(1925), in which he determines multiple solutions for a given requirement of movement transfer in a four-bar mechanism. Figure 4-6 presents a simplified version of his method. First, a point R is located at the intersection of the lines that describe an angle equal to the negative of half the range angle ψ_0 from point B_0 and the negative of half the dead-point angle φ_0 from point A_0
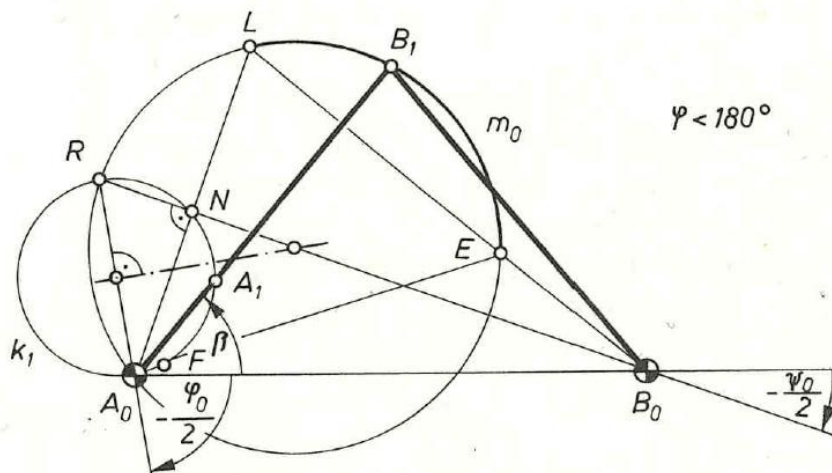
Figure 4-6 Graphic method for dead point based mechanism design.

(Image from Luck & Modler, 1995)

Then the circumferences k_1 and m_0 are drawn. Both must contain both points R and A_0, and their center points must be equidistant from R and A_0 as well. The center point for circumference k_1 must be located in the line $\overline{RA_0}$, while the line $\overline{RB_0}$ must contain the center point for circumference m_0. Those circumferences will contain the multiple solutions for the requirements of the mechanism at a dead point, k_1 containing point A_1,

the joint between the driver and transfer elements; and m_0 containing point B_1, the joint between the transfer and driven elements.

To define the arc sections of the circles k_1 and m_0 in which the solutions are located, a line that describes the negative of the range angle must be drawn from B_0. It intersects circumference m_0 in points E and L and the solution for point B_1 will be located in the arc limited by these two points. From points E and L, lines are drawn with point A₀ at the other end. The intersection of line $\overline{EA_0}$ and circumference k_1 defines point N, while the intersection of line $\overline{LA_0}$ and circumference k1 defines point F. Therefore, the solution for point A_1 is located in the arc limited by points N and F. A solution angle β is defined by the angle formed by the driver and transfer elements at its first dead-point state, with the fixed base $\overline{A_0B_0}$.

4.1.2 Kinematic calculations through numerical methods

To calculate the kinematic behavior of a mechanism, it is required to define restriction equations between its elements. The elements of a mechanism are mathematically described by their known parameters, like dimensions, fixed positions, or a fixed angle, and by unknown variables, like the angle between elements, moving points (i.e., joints), and variable lengths between elements. For example, in the mechanism shown in figure 4-7, the parameters are the element length L_1 and L_2, fixed positions A and B, and variables are the angles γ_1 and γ_2, and the length s.
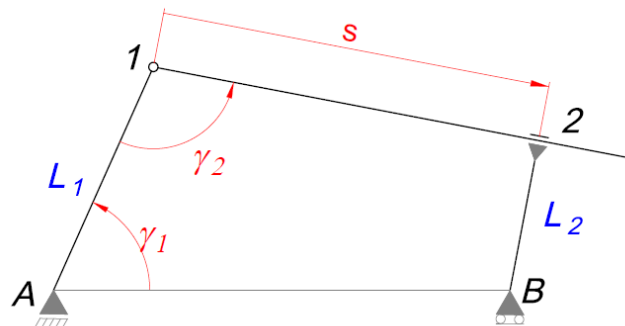
Figure 4-7 Example of four-bar mechanism with unknown variables.

(Image adapted from Meneses, 2019a)

These variables are selected according to the calculation requirements for the mechanism. Considering all joints between mechanism elements as variables is recommended because it simplifies the restriction equations. Additional points of interest can be considered as variables, as well as linear or angular displacements between elements of the mechanism. It is required that the conducting movement of the mechanism (i.e., the angular position of an electric motor shaft) is always included as a variable since it is required for the position, speed, and acceleration calculations.

The number of restrictions required is defined by the difference between the number of unknown variables "n" and the number of Degrees of Freedom (DOF) in the mechanism.

For example, we can evaluate the number of restrictions "r" required by the mechanism in figure 4-4. The unknown variables are γ_1, γ_2, and s, and the DOF of this kind of mechanism is 1. In this case, the number of restrictions required is defined as $r = n - DOF = 3 - 1 = 2$.

The restrictions can be expressed as mathematical equations composed of the different variables and known parameters. These expressions must be equated to zero to be arranged in a vectorial form. For example, in figure 4-8, given the length in the element $\overline{A1}$ and the fixed-point A, a position restriction can be established for the variables x1 and y1, as shown in equation (4.1).
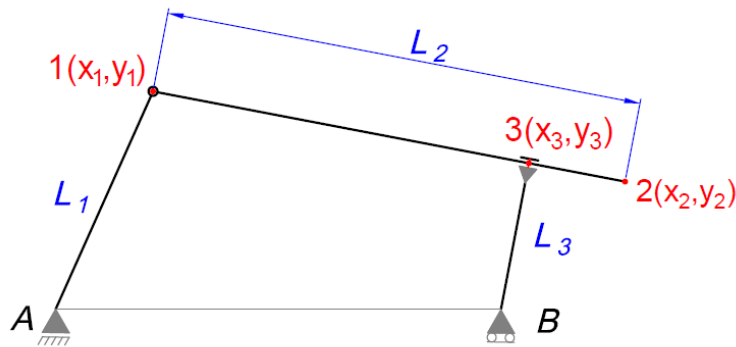
Figure 4-8 Example of four-bar mechanism with set point variables.

(Image adapted from Meneses, 2019a)

$$(x_1 - x_A)^2 + (y_1 - y_A)^2 - L_1^2 = 0 \ (4.1)$$

As another example, in figure 4.9, given the distance between point A and the point 1, and the fixed-point A, trigonometrical relations (4.2) and (4.3) can be established between the variable positions x_1 and y_1, the angle φ_1, and known length L_1.
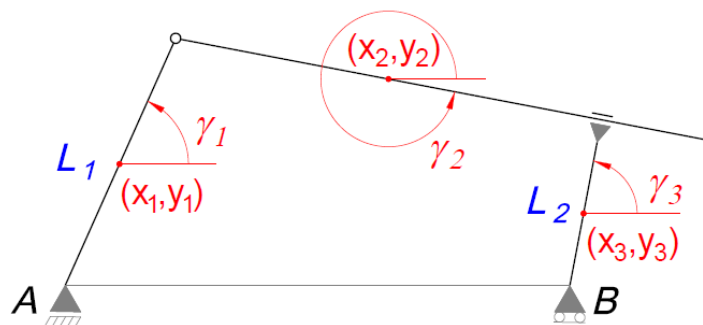
Figure 4-9 Example of four-bar mechanism with angular variables.

(Image adapted from Meneses, 2019a)

$$(x_1 - x_A) - \frac{L_1}{2}\cos\varphi_1 = 0 \quad (4.2)$$

$$(y_1 - y_A) - \frac{L_1}{2}\sin\varphi_1 = 0 \quad (4.3)$$

These trigonometrical relations are redundant, because both of them are establishing a relation between the angle and the same point, albeit through a different variable. This means only one of these relations can be used in the calculations. The decision is taken based on the trigonometrical function's sensibility to variation, which depends on the angle. For angles between 45° to 135° and 225° to 315° degrees, it's better to use the function $\cos(\gamma)$, because in this range, this function's value varies significantly from one degree to the next. For the rest of the angle range there is less variation in value an that can lead to problems in the algorithm, so the function $\sin(\gamma)$ is preferable.

The restriction equations defined are organized in a vector arrangement $\bar{\phi}$. The notation process is shown using equation (4.1) as an example. The restriction is assigned as a function that equals zero (4.4). This restriction function is then arranged in the resulting restriction vector $\bar{\phi}$ (4.5) alongside the other "r" restrictions.

$$\phi_1(x_1, y_1) = (x_1 - x_A)^2 + (y_1 - y_A)^2 - L_1^2 = 0 \quad (4.4)$$

$$\bar{\phi} = \begin{bmatrix} \phi_1 \\ \vdots \\ \phi_r \end{bmatrix} = \begin{bmatrix} 0 \\ \vdots \\ 0 \end{bmatrix} \quad (4.5)$$

Similarly, the variables of the system are organized as vector $\bar{q}$. This arrangement will have a (1 x n) size, being "n" the number of variables being calculated. Due to calculation requirements, the variable related to the conducting movement must be the q_n member of the vector. The vector notation is shown in expression (4.6).

$$\bar{q} = \begin{bmatrix} q_1 \\ \vdots \\ q_n \end{bmatrix} \quad (4.6)$$

With both vectors defined, it is possible to express the restriction vector as a function of the variable vector. The notation is shown in equation (4.7) and will be the basis for the position, speed, and acceleration calculations.

$$\bar{\phi}(\bar{q}) = \begin{bmatrix} \phi_1(\bar{q}) \\ \vdots \\ \phi_r(\bar{q}) \end{bmatrix} = \begin{bmatrix} 0 \\ \vdots \\ 0 \end{bmatrix} \quad (4.7)$$

To calculate the value of each variable during the displacement of the mechanism and the rate of change of said variables in time, an iterative process is developed based on the approximation of a solution to the equation (4.7). This iteration algorithm is summarized in figure 4.10. The characteristics of the conducting movement, such as position, speed and acceleration, are important input data that will lead the calculation process.

Using the given value for the position of the conducting movement, it is possible to approximate a solution for this equation system through the Newton-Raphson method (Avello, 2014), a numerical iterative method based on Taylor Series. Acording to Enciclopedia Britannica (2022), "a Taylor Series, for a linear function, is defined as an expression of a function f – for which the derivatives of all orders exist – at a point "a" in the domain of f in the form of a power series, composed by a derivative evaluated in a, multiplied by the difference between point a and the variable x". For simplicity, it can be approximated as a single derivative term form, as shown in equation (4.8)

$$f(x) \cong f(a) + f'(a)(x - a) \quad (4.8)$$

In a Taylor Series for a single variable, the function in equation (4.8) is calculated considering an approximation point "a". In the case of our iteration system, the approximation point will be defined by the vector $\bar{q}^0$, shown the expression (4.9). Each term of this approximation vector corresponds to known values of all variables at a defined point.

$$\bar{q}^0 = \begin{bmatrix} q_1{}^0 \\ \vdots \\ q_n{}^0 \end{bmatrix} \quad (4.9)$$

Applying the Taylor series concept to each restriction's multivariable function, the resulting function (4.10) is composed of the value of the function in the approximation point vector plus n partial derivative terms, evaluated at the approximation point. As with all restriction equations, this approximation function is equated to zero.

$$\phi_i(q_1, q_2, \dots, q_n) \cong \phi_i(\bar{q}^0) + \frac{\partial \phi_i}{\partial q_1}\bigg|_{\bar{q}^0} (q_1 - q_1{}^0) +$$
$$\frac{\partial \phi_i}{\partial q_2}\bigg|_{\bar{q}^0} (q_2 - q_2{}^0) + \cdots + \frac{\partial \phi_i}{\partial q_n}\bigg|_{\bar{q}^0} (q_n - q_n{}^0) = 0 \quad (4.10)$$

Re-arranging the term of the function ϕ_i, for $i = 1 \rightarrow r$, evaluated in the approximation point, the resulting restriction equation has a structure like the one shown in (4.11). Considering that we have r number of restrictions, a matrix equation is arranged, as shown in expression (4.12) Solving this matrix equation will provide values for all variables q_1 to q_n.

$$\frac{\partial \phi_i}{\partial q_1}\bigg|_{\bar{q}^0}(q_1 - q_1{}^0) + \frac{\partial \phi_i}{\partial q_2}\bigg|_{\bar{q}^0}(q_2 - q_2{}^0) + \cdots + \frac{\partial \phi_i}{\partial q_1}\bigg|_{\bar{q}^0}(q_n - q_n{}^0) = -\phi_i(\bar{q}^0) \text{ (4.11)}$$

$$\begin{bmatrix} \frac{\partial \phi_1}{\partial q_1}\big|_{\bar{q}^0} & \cdots & \frac{\partial \phi_1}{\partial q_n}\big|_{\bar{q}^0} \\ \vdots & \ddots & \vdots \\ \frac{\partial \phi_r}{\partial q_1}\big|_{\bar{q}^0} & \cdots & \frac{\partial \phi_r}{\partial q_n}\big|_{\bar{q}^0} \end{bmatrix} \begin{bmatrix} q_1 - q_1{}^0 \\ \vdots \\ q_n - q_n{}^0 \end{bmatrix} = - \begin{bmatrix} \phi_1(\bar{q}^0) \\ \vdots \\ \phi_r(\bar{q}^0) \end{bmatrix} \text{(4.12)}$$

The final matrix equation has a notation shown in expression (4.13), The partial derivative matrix $\bar{\phi}_{\bar{q}}$, also known as Jacobian Matrix (4.14), multiplied by the difference between the unknown variable vector $\bar{q}$ and the known approximation point $\bar{q}^0$ equals the negative value of the restriction vector evaluated at the approximation point.

$$\bar{\phi}_{\bar{q}}(\bar{q}^0) \cdot (\bar{q} - \bar{q}^0) = -\bar{\phi}(\bar{q}^0) \text{ (4.13)}$$

$$\bar{\phi}_{\bar{q}}(\bar{q}^0) = \left[\frac{\partial \phi_i}{\partial q_j}\bigg|_{\bar{q}^0}\right] = \begin{bmatrix} \frac{\partial \phi_1}{\partial q_1}\big|_{\bar{q}^0} & \cdots & \frac{\partial \phi_1}{\partial q_n}\big|_{\bar{q}^0} \\ \vdots & \ddots & \vdots \\ \frac{\partial \phi_r}{\partial q_1}\big|_{\bar{q}^0} & \cdots & \frac{\partial \phi_r}{\partial q_n}\big|_{\bar{q}^0} \end{bmatrix} \text{(4.14)}$$

To calculate the rate of variation on the values of variables over time, also considered speed in the case of most variables, we start from the basis of equation (4.7). By deriving it, the resulting expression (4.15) features the Jacobian Matrix being multiplied by the vector of the derivate of the variables' values over time ($\dot{q}$).

$$\bar{\phi}_{\bar{q}}(\bar{q}) \cdot \dot{q} = 0 \text{ (4.15)}$$

Analyzing expression (4.15) for a single restriction, we separate the terms that relate to unknown variables $(1 \rightarrow r)$ from those that refer to known variables such as the conducting movement $(r + 1 \rightarrow n)$. The resulting equation (4.16) is then developed

further by rearranging the terms that relate to the known variables on the other side of the equation, as shown in expression (4.17)

$$\frac{\partial \phi_i}{\partial q_1}\bigg|_{\bar{q}^0} \cdot \dot{q}_1 + \cdots + \frac{\partial \phi_i}{\partial q_r}\bigg|_{\bar{q}^0} \cdot \dot{q}_r + \frac{\partial \phi_i}{\partial q_{r+1}}\bigg|_{\bar{q}^0} \cdot \dot{q}_{r+1} + \cdots + \frac{\partial \phi_i}{\partial q_n}\bigg|_{\bar{q}^0} \cdot \dot{q}_n = 0 \quad (4.16)$$

$$\frac{\partial \phi_i}{\partial q_1}\bigg|_{\bar{q}^0} \cdot \dot{q}_1 + \cdots + \frac{\partial \phi_i}{\partial q_r}\bigg|_{\bar{q}^0} \cdot \dot{q}_r = -\left(\frac{\partial \phi_i}{\partial q_{r+1}}\bigg|_{\bar{q}^0} \cdot \dot{q}_{r+1} + \cdots + \frac{\partial \phi_i}{\partial q_n}\bigg|_{\bar{q}^0} \cdot \dot{q}_n \right) \quad (4.17)$$

This derivative form of the restrictions (4.17) is then arranged in a matrix structure, as shown in expression (4.18). At each side of the equation, we have sections of the Jacobian matrix corresponding to the variables they will multiply. The Jacobian matrix terms are evaluated at the approximation point $\bar{q}^0$. The variable vector is the only unknown part of the equation (4.18), so the expression can be solved.

$$\begin{bmatrix} \frac{\partial \phi_1}{\partial q_1}\big|_{\bar{q}^0} & \cdots & \frac{\partial \phi_1}{\partial q_r}\big|_{\bar{q}^0} \\ \vdots & \ddots & \vdots \\ \frac{\partial \phi_r}{\partial q_1}\big|_{\bar{q}^0} & \cdots & \frac{\partial \phi_r}{\partial q_r}\big|_{\bar{q}^0} \end{bmatrix} \begin{bmatrix} \dot{q}_1 \\ \vdots \\ \dot{q}_r \end{bmatrix} = - \begin{bmatrix} \frac{\partial \phi_1}{\partial q_{r+1}}\big|_{\bar{q}^0} & \cdots & \frac{\partial \phi_1}{\partial q_n}\big|_{\bar{q}^0} \\ \vdots & \ddots & \vdots \\ \frac{\partial \phi_r}{\partial q_{r+1}}\big|_{\bar{q}^0} & \cdots & \frac{\partial \phi_r}{\partial q_n}\big|_{\bar{q}^0} \end{bmatrix} \begin{bmatrix} \dot{q}_{r+1} \\ \vdots \\ \dot{q}_n \end{bmatrix} \quad (4.18)$$

The calculations for the acceleration values are done similarly to the speed calculations. By deriving equation (4.15), the resulting expression (4.19) is composed of the Jacobian Matrix $\bar{\phi}_{\bar{q}}(\bar{q})$ multiplied by the unknown acceleration values of the variables $\ddot{q}$, plus the partial derivate of the Jacobian Matrix, multiplied by the already known speed values $\dot{q}$.

$$\bar{\phi}_{\bar{q}}(\bar{q}) \cdot \ddot{q} + \dot{\phi}_{\bar{q}}(\bar{q}) \cdot \dot{q} = 0 \quad (4.19)$$

From expression (19) for a single restriction, once again we separate the terms that relate to unknown variables ($1 \rightarrow r$) from those that refer to the conducting movement ($r + 1 \rightarrow n$). The latter terms are added to the double summation of the terms of partial derivates (4.20).

$$\frac{\partial \phi_i}{\partial q_1}\bigg|_{\bar{q}^0} \cdot \ddot{q}_1 + \cdots + \frac{\partial \phi_i}{\partial q_r}\bigg|_{\bar{q}^0} \cdot \ddot{q}_r + \frac{\partial \phi_i}{\partial q_{r+1}}\bigg|_{\bar{q}^0} \cdot \ddot{q}_{r+1} + \cdots +$$

$$\frac{\partial \phi_i}{\partial q_n}\bigg|_{\bar{q}^0} \cdot \ddot{q}_n + \sum_{j=1}^{n}\sum_{i=1}^{r} \frac{\partial^2 \phi_i}{\partial q_i \partial q_j} \cdot \dot{q}_i \dot{q}_j = 0 \quad (4.20)$$

By rearranging the Jacobian Matrix terms related to the unknown variables of the restrictions on the right side, the resulting expression (4.21) forms a matrix equation $A \cdot b = C$, with the left side defined by already known data. By solving this equation, the acceleration values can be found.

$$
\begin{bmatrix} \frac{\partial \phi_1}{\partial q_1}\big|_{\bar{q}^0} & \cdots & \frac{\partial \phi_1}{\partial q_r}\big|_{\bar{q}^0} \\ \vdots & \ddots & \vdots \\ \frac{\partial \phi_r}{\partial q_1}\big|_{\bar{q}^0} & \cdots & \frac{\partial \phi_r}{\partial q_r}\big|_{\bar{q}^0} \end{bmatrix} \begin{bmatrix} \ddot{q}_1 \\ \vdots \\ \ddot{q}_r \end{bmatrix} = - \begin{bmatrix} \frac{\partial \phi_1}{\partial q_{r+1}}\big|_{\bar{q}^0} & \cdots & \frac{\partial \phi_1}{\partial q_n}\big|_{\bar{q}^0} \\ \vdots & \ddots & \vdots \\ \frac{\partial \phi_r}{\partial q_{r+1}}\big|_{\bar{q}^0} & \cdots & \frac{\partial \phi_r}{\partial q_n}\big|_{\bar{q}^0} \end{bmatrix} \begin{bmatrix} \ddot{q}_{r+1} \\ \vdots \\ \ddot{q}_n \end{bmatrix} - \begin{bmatrix} \sum_{j=1}^{n} \sum_{i=1}^{r} \frac{\partial^2 \phi_1}{\partial q_i \partial q_j} \cdot \dot{q}_i \dot{q}_j \\ \vdots \\ \sum_{j=1}^{n} \sum_{i=1}^{r} \frac{\partial^2 \phi_r}{\partial q_i \partial q_j} \cdot \dot{q}_i \dot{q}_j \end{bmatrix} \quad (4.21)
$$

To calculate the movement of a given mechanism, and the values of speed and acceleration of the established variables of the vector $\bar{q}$, the iteration algorithm is applied through a calculation program written in MATLAB. The steps that the algorithm follows are explained in the flowchart shown in figure 4-10.
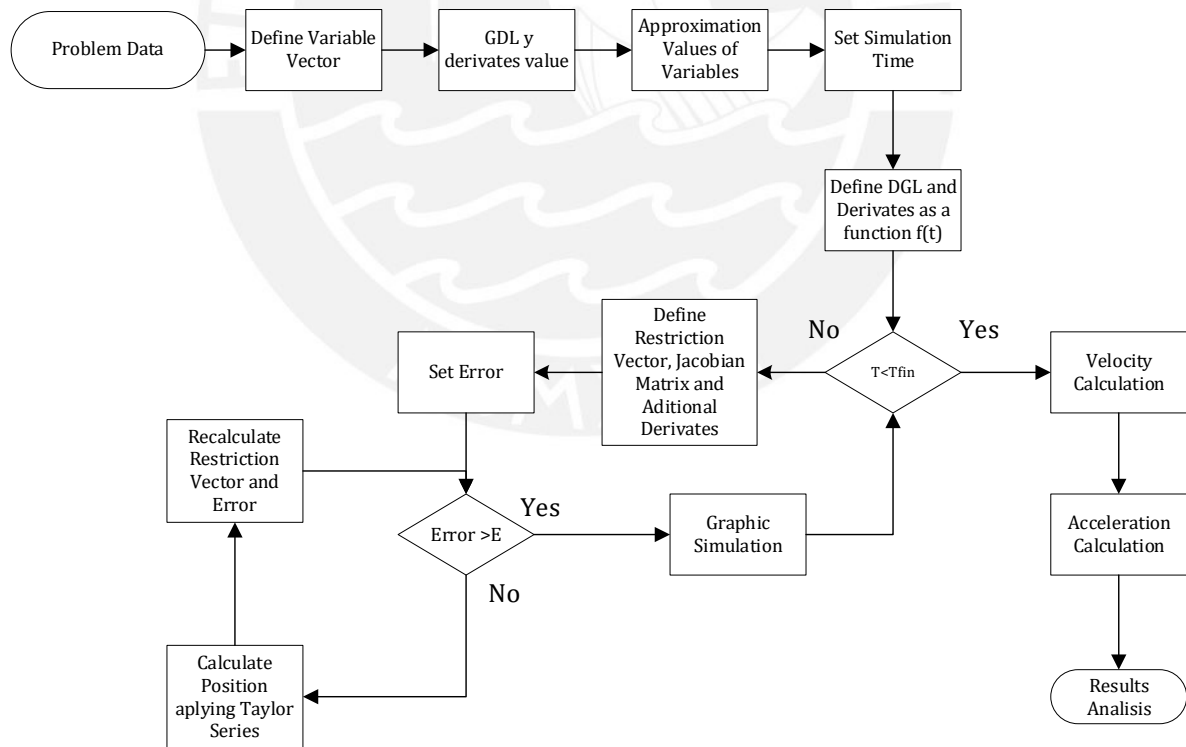
Figure 4-10 Flow chart of cinematic calculation program.

(Image adapted from Meneses, 2019b)

For this program, it is required to know the speed and acceleration of the conducting movement, as well as a function of its position. Also, an approximation point is required, which in this case will be one of the dead points of the mechanism's movement. Furthermore, the code also requires the restriction vector, the Jacobian Matrix, and the vector formed by the summation of the partial derivates of the Jacobian Matrix.

The code also must consider modifications if trigonometrical restrictions are being used, since a low sensitivity to change in these restrictions can lead to a non-convergent system. To solve this, the code can use the angle value of the previous iteration to select the right trigonometrical function, considering the absolute value of the angle's tangent to decide. If this value is above 1, function cos is used, otherwise the selected functions will be sin.

Additional settings required for the internal process of the program are explained in the Annex I: Kinematic Calculations Program Code at the end of the document.

4.2 Synthesis of actuation mechanism

With the mechanism type and morphology defined, the next step is calculating the mechanism dimensions. For this, the graphic method of mechanism synthesis explained in section 4.1.1 is applied. The angle between the first and second dead-point states for this mechanism will be considered in $\varphi_0=160º$ for the driver element, because it is kinematically impossible to have a mechanism with a dead-point in $\varphi_0=180º$ (TU-Ilmenau, 2020b), and closer the angle is to this point, the harder it is for the system to move. Angles bigger than $\varphi_0=180º$ are possible, but demand bigger mechanisms. The range of movement of the driven element was previously defined as $\psi_0=45º$, and shown in the movement transfer function in figure 4-11. The graphic procedure for the multiple mechanism solutions is shown in figure 4-12.
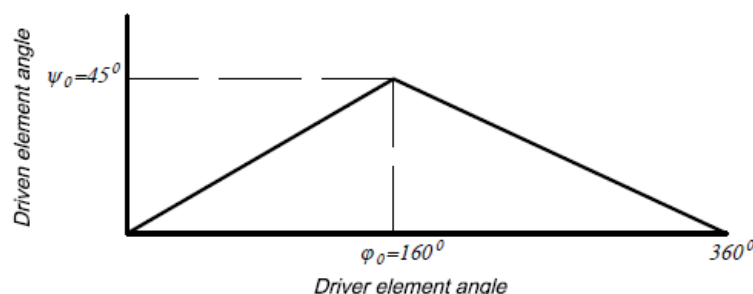
Figure 4-11 Movement transfer function of the mechanism.
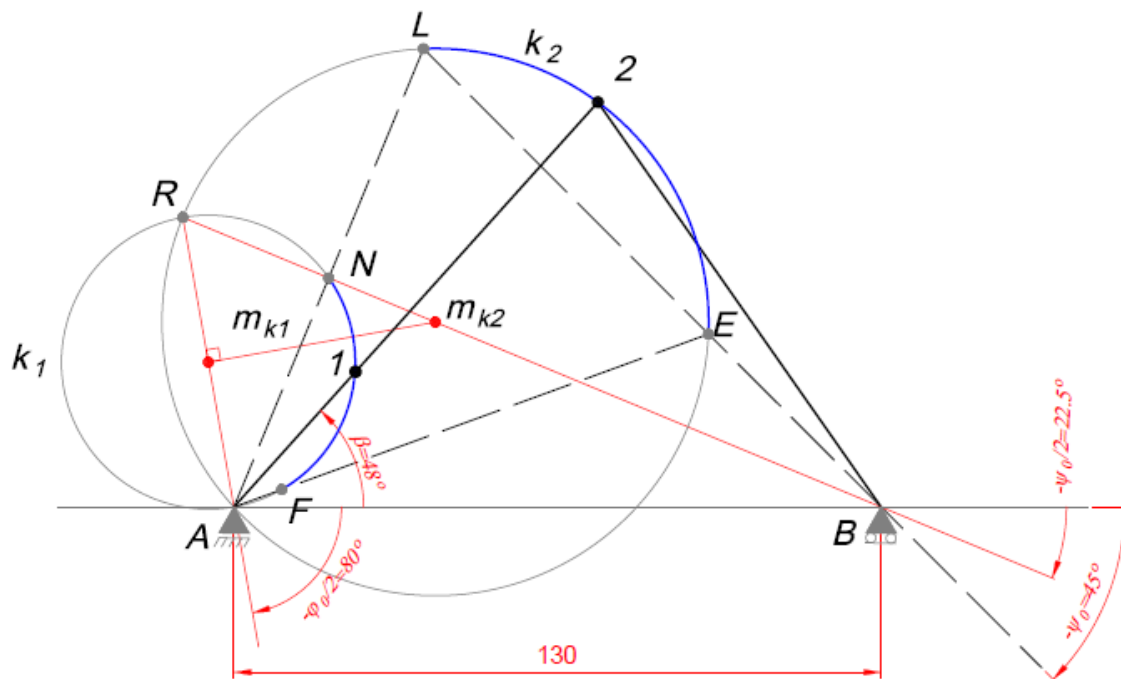
Figure 4-12 Design of the mechanism by dead point graphic method.

The transmission angle criterion can be applied to optimize the solution selected from the options given by the graphic dead-point method (Marx, 1994). The transmission angle is defined by the angle between the tangents to the transmission element and the driven element movements. Coincidentally, it is also the angle between said elements. The criterion is based on the minimum transmission angle (μ_{min}) for the dead-point states being located on the first one. The mechanism is considered optimized if the maximum angle μ_{min} ($max\mu_{min}$) is selected. To achieve this, the tabulated curves displayed in figure 4-13 yield the value of $max\mu_{min}$ and the respective solution angle β. The input for these curves is the angle between dead-points of the driver element (φ_0) and the range of the driven element (ψ_0).
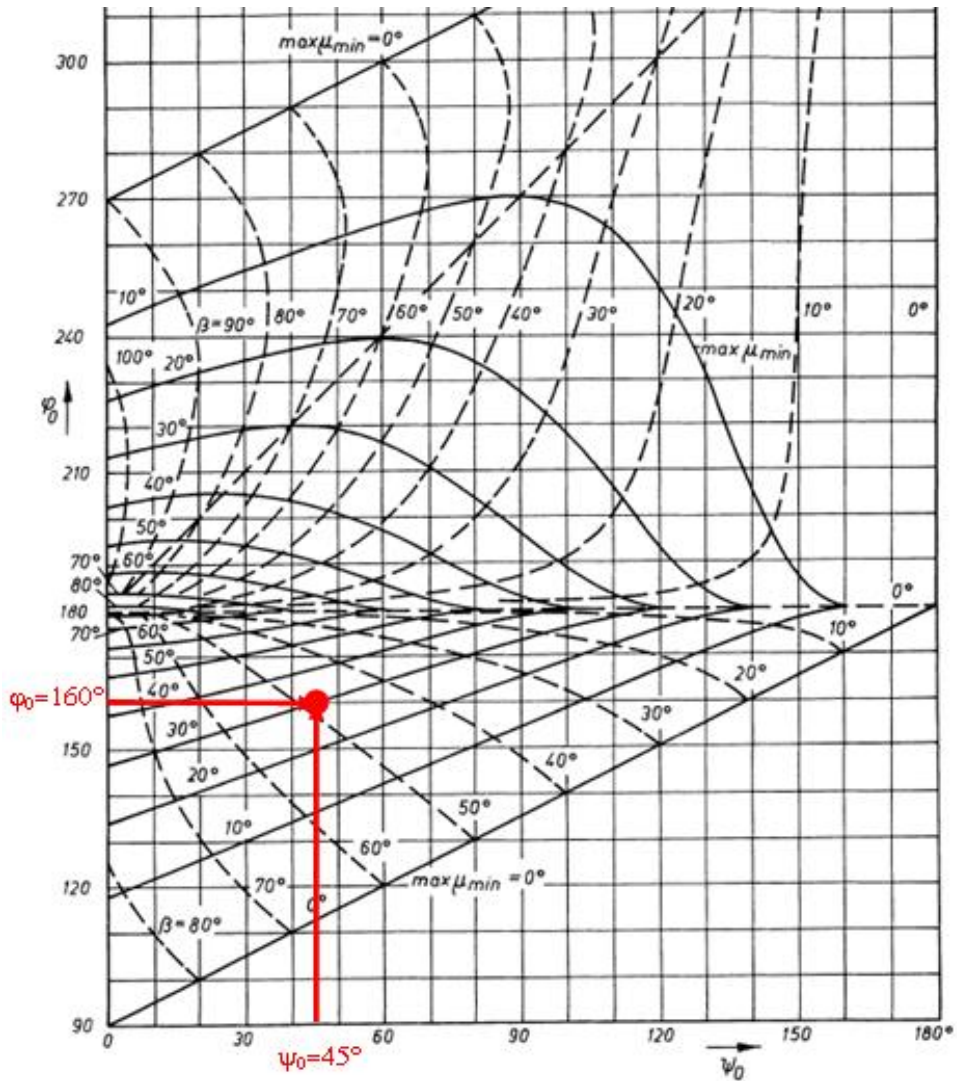
Figure 4-13 Tabulated curves for the maximum minimal angle of transmision.

(Image from Luck & Modler, 1995)

For the angles $\varphi_0{=}160°$ and $\psi_0{=}45°$, the values obtained in the tabulated curves are $max\mu_{min} = 30^o$ and $\beta = 48^o$. Taking the value of β into the figure 4-13, the measures obtained for the mechanism's elements are $\overline{A1} = 36.316mm$, $\overline{12} = 72.962\ mm$, and $\overline{2B} = 99.147\ mm$. To facilitate the fabrication process of the mechanism, the dimensions obtained through the graphic method are rounded to their final dimensions shown in figure 4-14.
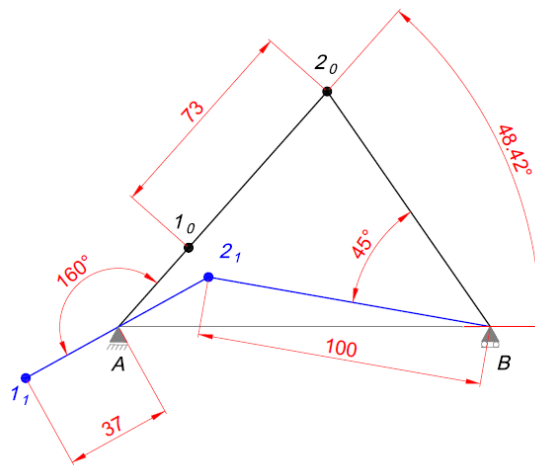
Figure 4-14 Final dimensions of the four-bar mechanism in both dead-point states

4.3 Kinematic analysis of the mechanism

For the designed mechanism, certain variables are important for calculating its position along with the movement range, speed, and acceleration over time. For this, the numerical method analysis explained in section 4.1.2 will be applied by establishing variables of interest and defining restriction functions in conjunction with known parameters from the design process.

The list below describes the points of interest to be calculated. Each point is composed of two variables, its coordinates in x and y. The variables are is shown in red in figure 4-15.

1. The joint between the input crank and the floating link $(x_1; y_1)$
2. The joint between the floating link and the output crank $(x_2; y_2)$
3. The middle mobile contact point $(x_3; y_3)$
4. The angle between the horizontal axis and the arm $\overline{2B}$ of the driven element (θ)
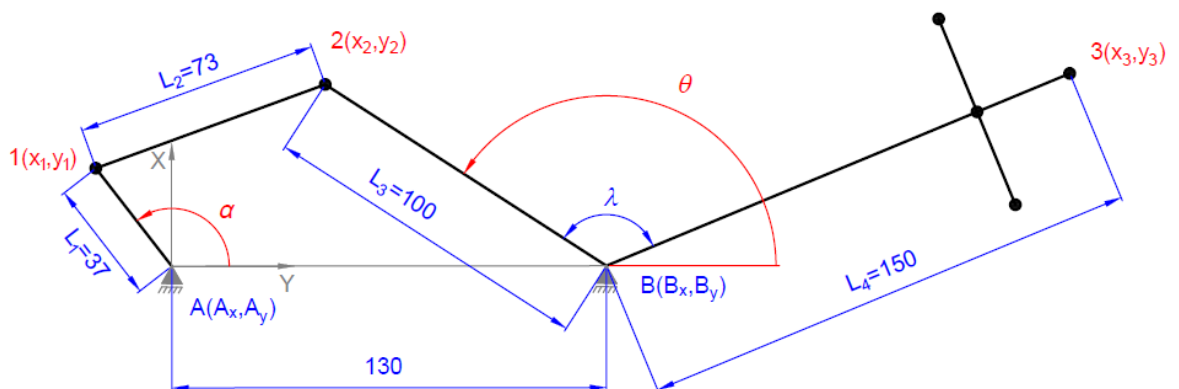
Figure 4-15 Mechanism with variables (red) and parameters (blue)

The other variable that must be considered is the angle α between the horizontal line and the input crank because it is associated with the conducting movement of the electric motor. Angle α is also shown in figure 4-15. These variables are arranged in vector $\bar{q}$ shown in expression (4.22). The known parameters of the mechanism displayed in blue in figure 4-15, where position A is (0,0) and position B is (130,0).

$$\bar{q} = \begin{bmatrix} x_1 \\ y_1 \\ x_2 \\ y_2 \\ x_3 \\ y_3 \\ \theta \\ \alpha \end{bmatrix} \text{ (4.22)}$$

Since the mechanism has 1 DOF and n=8 variables, the restriction system must be composed of r=7 restrictions. The restriction system, in its vector form, is shown in expression (4.23). It must be noted that, while some restriction functions may have multiple solutions, the systems will yield a correct and unique result for the system, if the initial approximation point was selected correctly. Also, since there are two trigonometrical restrictions, the function variants can also be used in the calculations and are shown in (4.24).

$$\bar{\phi} = \begin{bmatrix} (x_1 - x_A)^2 + (y_1 - y_A)^2 - L_1^2 \\ (x_2 - x_1)^2 + (y_2 - y_1)^2 - L_2^2 \\ (x_2 - x_B)^2 + (y_2 - y_B)^2 - L_3^2 \\ (x_3 - x_B)^2 + (y_3 - y_B)^2 - L_4^2 \\ (x_2 - x_B)(x_3 - x_B) + (y_2 - y_B)(y_3 - y_B) - L_3 \cdot L_4 \cdot \cos(\lambda) \\ (x_2 - x_B) - L_3 \cos(\theta) \\ (x_1 - x_A) - L_1 \cos(\alpha) \end{bmatrix} = \begin{bmatrix} 0 \\ 0 \\ 0 \\ 0 \\ 0 \\ 0 \\ 0 \end{bmatrix} \text{ (4.23)}$$

$$\begin{bmatrix} (y_2 - y_B) - L_3 \sin(\theta) \\ (y_1 - y_A) - L_1 \sin(\alpha) \end{bmatrix} = \begin{bmatrix} 0 \\ 0 \end{bmatrix} \text{ (4.24)}$$

For these calculations, it is needed to determine the Jacobian matrix of the restriction vector, which is shown in equation (4.25). The trigonometrical variants are also considered, and shown in (4.26)

$$\bar{\phi}_{\bar{q}}(\bar{q}^0) = \begin{bmatrix} 2(x_1 - x_A) & 2(y_1 - y_A) & 0 & 0 & 0 & 0 & 0 & 0 \\ -2(x_2 - x_1) & -2(y_2 - y_1) & 2(x_2 - x_1) & 2(y_2 - y_1) & 0 & 0 & 0 & 0 \\ 0 & 0 & 2(x_2 - x_B) & 2(y_2 - y_B) & 0 & 0 & 0 & 0 \\ 0 & 0 & 0 & 0 & 2(x_3 - x_B) & 2(y_3 - y_B) & 0 & 0 \\ 0 & 0 & (x_3 - x_B) & (y_3 - y_B) & (x_2 - x_B) & (y_2 - y_B) & 0 & 0 \\ 0 & 0 & 1 & 0 & 0 & 0 & L_1 \sin(\theta) & 0 \\ 1 & 0 & 0 & 0 & 0 & 0 & 0 & L_1 \sin(\alpha) \end{bmatrix} \quad (4.25)$$

$$\begin{bmatrix} 0 & 0 & 0 & 1 & 0 & 0 & -L_1 \cos(\theta) & 0 \\ 0 & 1 & 0 & 0 & 0 & 0 & 0 & -L_1 \cos(\alpha) \end{bmatrix} \quad (4.26)$$

Also, an approximation point must be established, as is shown in equation (4.27). Finally, position variables are shown in millimeters, and angles α and θ are shown in radians. This values correspond to the first dead point position of the mechanism.

$$\bar{q}^0 = \begin{bmatrix} x_1^0 \\ y_1^0 \\ x_2^0 \\ y_2^0 \\ x_3^0 \\ y_3^0 \\ \theta^0 \\ \alpha^0 \end{bmatrix} = \begin{bmatrix} 24 \\ 27 \\ 73 \\ 82 \\ 280 \\ 0 \\ 2.177 \\ 0.83 \end{bmatrix} \quad (4.27)$$

The double summation that relates to the term $\dot{\phi}_{\bar{q}}(\bar{q}) \cdot \dot{q}$, is shown in expression (4.28). The trigonometrical variation are considered in (4.29)

$$\bar{\phi} = \begin{bmatrix} 2\dot{x}_1^2 + 2\dot{y}_1^2 \\ 2((\dot{x}_1 - \dot{x}_2)^2 + (\dot{y}_1 - \dot{y}_2)^2) \\ 2\dot{x}_2^2 + 2\dot{y}_2^2 \\ 2\dot{x}_3^2 + 2\dot{y}_3^2 \\ 2(\dot{x}_2 \cdot \dot{x}_3 + \dot{y}_2 \cdot \dot{y}_3) \\ L_3 \cos(\theta) \cdot \dot{\theta}^2 \\ L_1 \cos(\alpha) \cdot \dot{\alpha}^2 \end{bmatrix} \quad (4.26)$$

$$\begin{bmatrix} L_3 \sin(\theta) \cdot \dot{\theta}^2 \\ L_1 \sin(\alpha) \cdot \dot{\alpha}^2 \end{bmatrix} \quad (4.29)$$

46

The conductive movement, which is the rotation of the driver element around point A, is dictated by a constant 50 R.P.M. electric motor (fig. 4.4), or its equivalent, 5.23 rad/s. Using this data, the MATLAB program can define the position, speed, and acceleration of all the previously defined variable points. For example, figure 4-16 shows the angular position, speed, and acceleration graphics for the driven angle θ. The x-axis for this graphic is the angular displacement for the driver element, the driver angle α. From the results of the driven angle, it is possible to calculate the kinematic values of any point of the extended driven element through simple calculations of the rigid solid kinematic. The results for all variables is presented in Annex II: Kinematic Calculation Results.
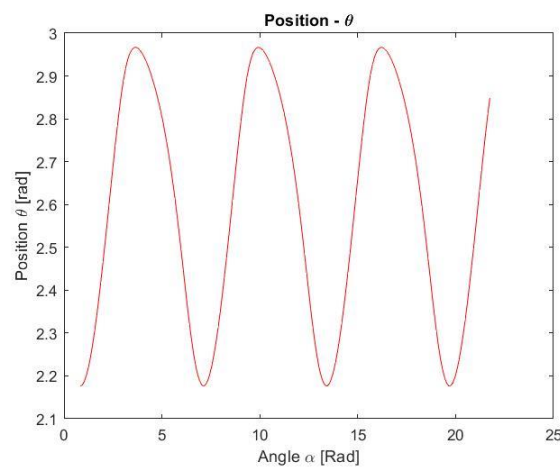
Figure 4-16 Angular position of the driven element θ vs angular position of the driver element α

Figure 4-16 shows the angular range of movement of the driven element. It forms a ciclic movement, that goes along the rotation of the driver element. When reviewed alongside figure 4-17, it can be noted that the extreme positions of the driven element's range coincide with the dead points established in section 4.2.1, since the angular speed for this positions is zero. Each cicle registers only 2 points in which the angular speed of the driven element is zero, in accordance to the synthesis theory.
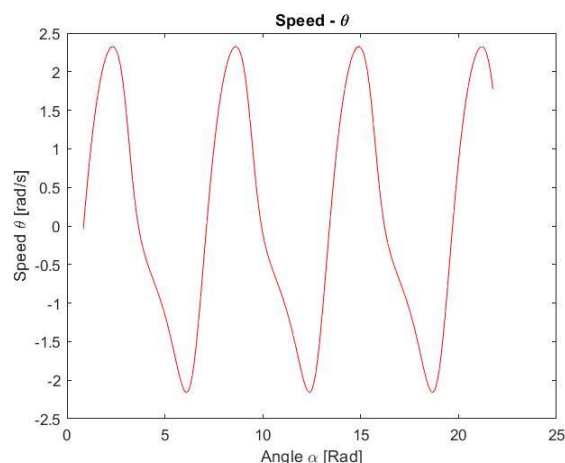
Figure 4-17 Angular speed of the driven element $\dot{\theta}$ vs angular position of the driver element α

It can also be noted, that dead-points of the mechanism's movement coincide with the points of maximum acceleration, as shown in figure 4-18. In calculations that requires
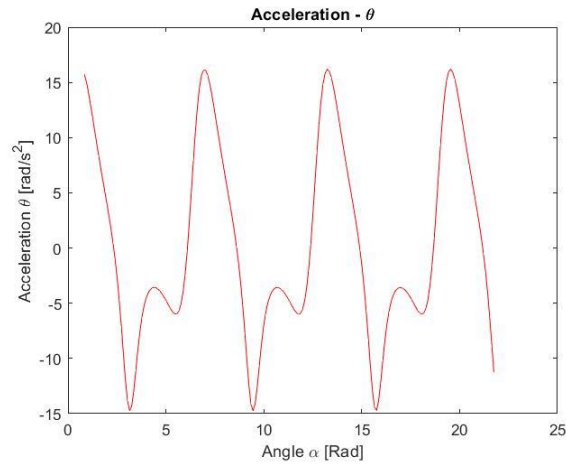
Figure 4-18 Angular acceleration of the driven element $\ddot{\theta}$ vs angular position of the driver element α

5 Prototype and achieved movement

Through the mechanism synthesis calculations, the dimensions of the concept of the mechanism are established. With this values, it is possible to build said mechanism and test the possibility of magnetic actuation on the soft tensegrity structure.

5.1 Prototype construction and description

The prototype for the actuation mechanism is built by a 3D-printing process. The construction material is PLA, the same as the mold material. The mechanism, shown as a model in figure 5-1, consists of a fixed base (in yellow), a driver element (green), a transfer element (red), and the extended driven element (blue) linked to a T-shaped body (pink). An electric motor is housed in the fixed base. These parts have a transversal section of 7 mm. in height and 10 mm. in width.
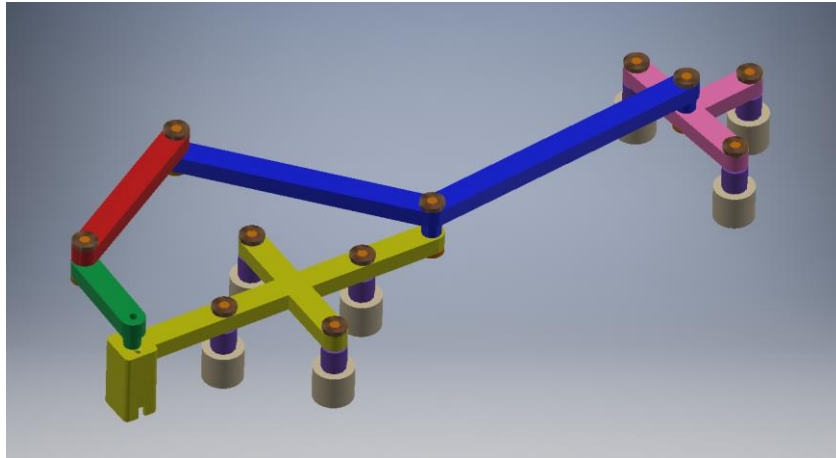
Figure 5-1 Actuation Mecanism (Inventor Model).

The mechanism elements are linked by 5mm pins glued on top to a fixating disc (figure 5-2 a). The magnetic contact points, both fixed and actuated, are formed by the magnet, a housing space, a pin, a separator, and a fixating disc (Figure 5-2 b)
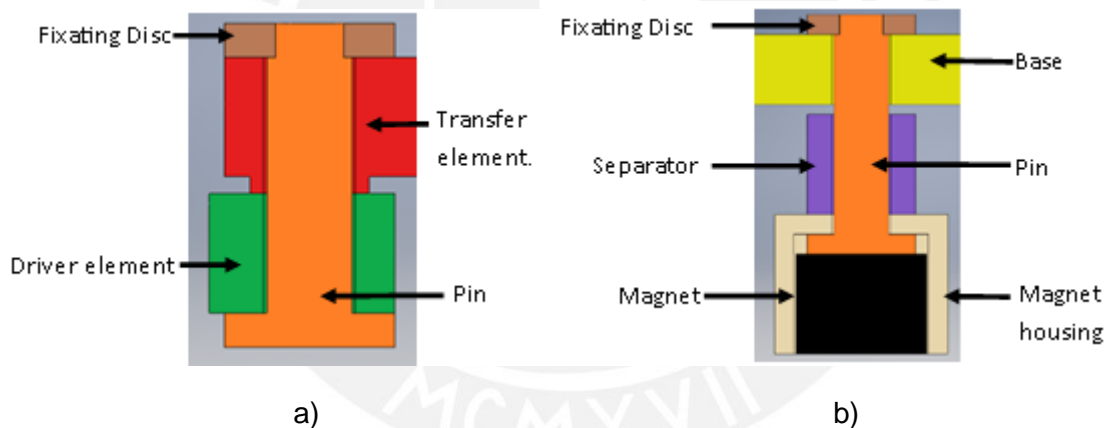
Figure 5-2 Transversal sections of a) articulation link b) magnetic link point.

The electric motor's shaft has an interference conection with the driver element of the mechanism. It is also connected to a 9v. battery and an interruptor in a serial configuration.

5.2 Assembly of the experiment

The experiment consists of linking the STS to the actuating mechanism in the linking points described in section 4. This magnetic link is done between the magnetic components of the STS and the magnet that is being housed in the actuating mechanism through a 2mm polycarbonate panel. The STS Is located above the polycarbonate panel, which is in a horizontal position, while the actuating mechanism is below. Therefore, the

panel must be supported high enough, so the mechanism has no movement interference. This configuration can be observed in figure 5-3.

a)   b)
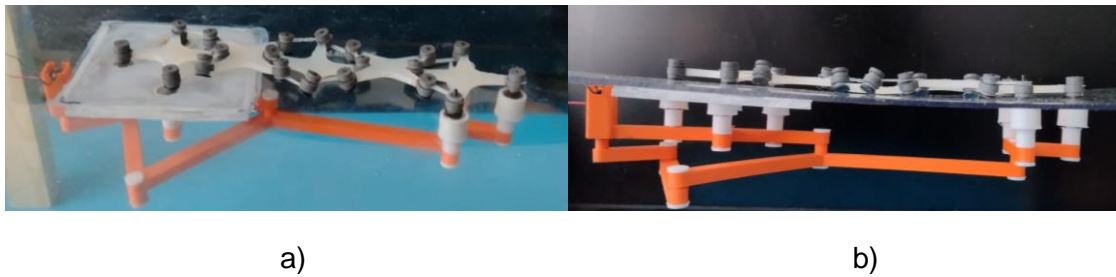
Figure 5-3 Experiment assembly: a) elevated view b) lateral view

To keep the fixed link points in position, the panel has a socket arrangement (figure 5-4) that keeps them, and in consequence fixed base of the mechanism, from moving. Before the assembly process, it is important to lubricate the surface over which the elastomer structure will move. Holding the mechanism upside-down and in position, the STS is located, with the magnetic terminals in the first member of the structure matching the magnets of the mechanism in the fixed position. The magnetic terminals of the structure's fifth member are positioned above the actuating magnets on the other side of the mechanism. Finally, the cables that connect the electric motor to its battery must be secured outside the range of movement of the input crank of the mechanism.
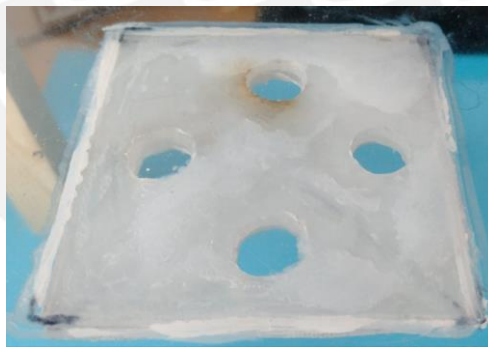
Figure 5-4 Fixing socket arrangement

5.3 Achieved movement

When the electric motor is turned on, the mechanism begins its natural movement, driving the soft tensegrity structure along the way through the polycarbonate panel. The movement achieved by the driven Soft Tensegrity Structure is an oscillatory angular movement that goes from a straight to a curved position.

In figure 5-5, the system is shown in the first dead point, which corresponds to the straight position of the STS. The driver and transmission elements are shown in a colinear

position, while the structure is kept in a linear configuration by the actuating magnetic link points.
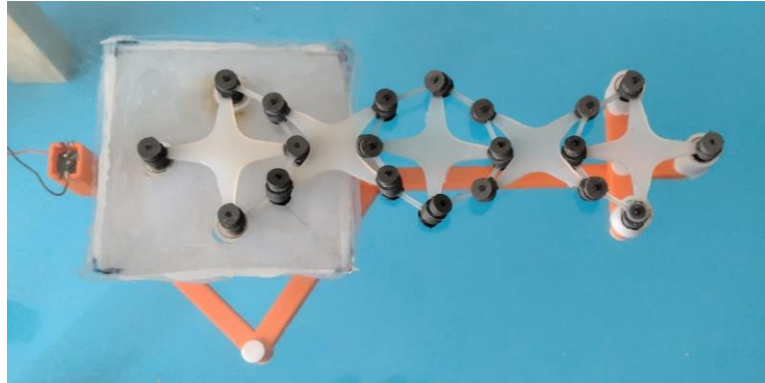
Figure 5-5 System in first dead point – straight position

In figure 5-6, the driver element shows an angular displacement in a clockwise direction in the middle of the two dead points. The mechanism has driven the structure to a lightly bent configuration, in which curvature is barely visible..

Figure 5-6 System in a middle point

In figure 5-7, the Soft Tensegrity Structure has reached its final bent configuration, while the mechanism is shown in its second dead point. The bending angle in the structure is 45o degrees, as was proposed in section 2.1 and detailed in section 4. The STS also presents a curvature generated by the configuration of pre-stressed tension elements shown in figure 2-3. From here, the driver element of the mechanism completes its rotation while the driven element and the STS return to the initial straight configuration.
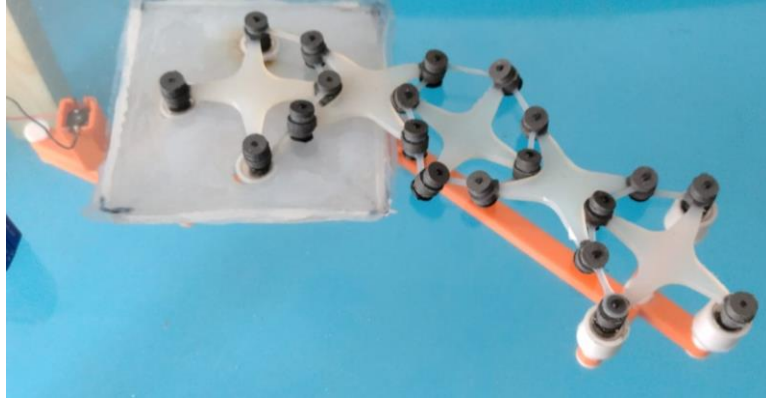
Figure 5-7 System in second dead point, bent 45° degrees

Some aspects to consider from this experiment are the effect of the mechanism position on the stability of the assembly and the effect of the pre-stressed tension element configuration.

In figure 5-3 b), the actuation mechanism is shown upside down. This means that the attraction force between the magnets and the MREs must also keep the mechanism in its position. Therefore, at certain times, the combined action of the weight and the mechanism's movement de-linked the magnets from the structure.

While this was not common with the configuration presented in figure 2-6, it happened more frequently when a structure design that contained more 12.5 mm. long tension elements were tested. This also means that the pre-stress configuration of the structure can benefit or difficult the actuation movement and its stability.

6   Conclusions and future work

6.1   Conclusions

The main goal of this thesis was to show the possibility of a magnetically actuated movement on a soft tensegrity structure through a barrier that separates the structure from the source of magnetic actuation. The mechanism prototype described in section 5 of this work achieved a 45° degrees angular oscillating movement in an STS that initially has a linear arrangement. This mechanism is linked to the structure through magnets that exert an attraction force to the magneto-rheological elastomer parts of the STS. Both the mechanism that houses the magnets and the STS that is affected by them are separated by a 2 mm. polycarbonate panel.

While the objective of a magnetically actuated movement was achieved, some considerations must be considered. The magnetic attraction force not only transmits the movement from the actuating mechanism to the soft tensegrity structure. It also must be strong enough to keep both elements linked, no matter their position.

The pre-stressed tension elements should also be taken into consideration. While an adecuate pre-stress can improve the performance of the actuation movement, an

excesive pre-stress can difficult some stages actuation movement, and even de-link the magnet from the MRE parts of the structure in some cases

Also, it was possible to calculate the kinematic values of specific points in the mechanism through numerical methods. This opens up the possibility of controlling the final movement of the structure through the kinematic calculation of the actuated magnetic link points.

6.2 Future work

While the present thesis could achieve a simple oscillating angular movement, achieving more controlled movements in future works would be interesting. For example, two symmetrical STS that could work in tandem as a gripper, controlled by step-by-step electric motors that are not in direct contact with the structure, is feasible.

Another possibility of study would be the analysis of the magnetic attraction force between a magnet and an MRE that are separated by a physical barrier and the effect of the width of said barrier on this attraction force.

The cuantification of the effect of different pre-stressed configurations in a given actuated movement of an STS could be an interesting topic of study as well.

Also, during the fabrication process, it was noted that vibrations could help in the degassing of the elastomer mixture. This topic could be studied to allow degasification of the elastomer elements while in the mold. This method is being explored by H. Wang et al.(2019) through ultrasonic vibrations, but mechanical vibrations are also an option to consider.

ANNEX I: Kinematic calculations program code

```
%script to calculate the cinematic of a
%four-bar mechanism
close all
%Parameters
L1=37;L2=73;L3=100;L4=150;Lambda=2.177;xA=0;yA=0;xB=130;yB=0;
% value of GDL and derivates
alpha0=0.83;w=5.23;a=0;
%initial aproximation
x1=24;y1=27;x2=73;y2=82;x3=280;y3=0;theta=2.177;
%tiempo
N=200;tfin=4;
% Variables Vector
q=[x1;y1;x2;y2;x3;y3;theta;alpha0];

% Vectors to store the positions of points 1, 2, 3,
% and angles ALPHA and THETA
X1=zeros(N,1); Y1=zeros(N,1);
X2=zeros(N,1); Y2=zeros(N,1);
X3=zeros(N,1); Y3=zeros(N,1);
ALPHA=zeros(N,1); THETA=zeros(N,1);

% Vectors to store the speed of points 1, 2, 3,
% and angle Theta
x1p=zeros(N,1); y1p=zeros(N,1);
x2p=zeros(N,1); y2p=zeros(N,1);
x3p=zeros(N,1); y3p=zeros(N,1);
THETAp=zeros(N,1);

% Vectors to store the acceleration of points 1, 2, 3,
% and angle Theta
x1pp=zeros(N,1); y1pp=zeros(N,1);
x2pp=zeros(N,1); y2pp=zeros(N,1);
x3pp=zeros(N,1); y3pp=zeros(N,1);
THETApp=zeros(N,1);

%Time loop
for i=1:N
    t=tfin*(i-1)/(N-1);
    alpha=alpha0+w*t+0.5*a*t^2; q(8)=alpha;
    alphap=w+a*t;
    %Position Problem
    %Initial error calculation
    %Condition for sensitivity to variation on angle ALPHA
    if abs(tan(alpha))<1
        %Condition for sensitivity to variation on angle THETA
        if abs(tan(theta))<1
            phi=[(x1-xA)^2+(y1-yA)^2-L1^2;
            (x2-x1)^2+(y2-y1)^2-L2^2;
            (x2-xB)^2+(y2-yB)^2-L3^2;
            (x3-xB)^2+(y3-yB)^2-L4^2;
            (x2-xB)*(x3-xB)+(y2-yB)*(y3-yB)-L3*L4*cos(Lambda);
            (y2-yB)-L3*sin(theta);
            (y1-yA)-L1*sin(alpha)];
        else
            phi=[(x1-xA)^2+(y1-yA)^2-L1^2;
```

```
            (x2-x1)^2+(y2-y1)^2-L2^2;
            (x2-xB)^2+(y2-yB)^2-L3^2;
            (x3-xB)^2+(y3-yB)^2-L4^2;
            (x2-xB)*(x3-xB)+(y2-yB)*(y3-yB)-L3*L4*cos(Lambda);
            (x2-xB)-L3*cos(theta);
            (y1-yA)-L1*sin(alpha)];
        end

    else
        %Condition for sensitivity to variation on angle THETA
        if abs(tan(theta))<1
            phi=[(x1-xA)^2+(y1-yA)^2-L1^2;
            (x2-x1)^2+(y2-y1)^2-L2^2;
            (x2-xB)^2+(y2-yB)^2-L3^2;
            (x3-xB)^2+(y3-yB)^2-L4^2;
            (x2-xB)*(x3-xB)+(y2-yB)*(y3-yB)-L3*L4*cos(Lambda);
            (y2-yB)-L3*sin(theta);
            (x1-xA)-L1*cos(alpha)];
        else
            phi=[(x1-xA)^2+(y1-yA)^2-L1^2;
            (x2-x1)^2+(y2-y1)^2-L2^2;
            (x2-xB)^2+(y2-yB)^2-L3^2;
            (x3-xB)^2+(y3-yB)^2-L4^2;
            (x2-xB)*(x3-xB)+(y2-yB)*(y3-yB)-L3*L4*cos(Lambda);
            (x2-xB)-L3*cos(theta);
            (x1-xA)-L1*cos(alpha)];
        end
    end
end
error=norm(phi);
%Newton-Raphson iterative loop
while error>1.e-08
    %Condition for sensitivity to variation on angle ALPHA
     if abs(tan(alpha))<1
        %Condition for sensitivity to variation on angle THETA
        if abs(tan(theta))<1
           Phiq=[2*(x1-xA) 2*(y1-yA) 0 0 0 0 0 0 ;
           -2*(x2-x1)  -2*(y2-y1)  2*(x2-x1) 2*(y2-y1) 0 0 0 0;
           0 0 2*(x2-xB) 2*(y2-yB) 0 0 0 0;
           0 0 0 0 2*(x3-xB) 2*(y3-yB) 0 0;
           0 0 (x3-xB) (y3-yB) (x2-xB) (y2-yB) 0 0;
           0 0 0 1 0 0 -L3*cos(theta) 0;
           0 1 0 0 0 0 0 -L1*cos(alpha)];
        else
           Phiq=[2*(x1-xA) 2*(y1-yA) 0 0 0 0 0 0 ;
           -2*(x2-x1)  -2*(y2-y1)  2*(x2-x1) 2*(y2-y1) 0 0 0 0;
           0 0 2*(x2-xB) 2*(y2-yB) 0 0 0 0;
           0 0 0 0 2*(x3-xB) 2*(y3-yB) 0 0;
           0 0 (x3-xB) (y3-yB) (x2-xB) (y2-yB) 0 0;
           0 0 1 0 0 0 L3*sin(theta) 0;
           0 1 0 0 0 0 0 -L1*cos(alpha)];
        end
     else
         %Condition for sensitivity to variation on angle THETA
        if abs(tan(theta))<1
            Phiq=[2*(x1-xA) 2*(y1-yA) 0 0 0 0 0 0 ;
            -2*(x2-x1)  -2*(y2-y1)  2*(x2-x1) 2*(y2-y1) 0 0 0 0;
            0 0 2*(x2-xB) 2*(y2-yB) 0 0 0 0;
            0 0 0 0 2*(x3-xB) 2*(y3-yB) 0 0;
            0 0 (x3-xB) (y3-yB) (x2-xB) (y2-yB) 0 0;
            0 0 0 1 0 0 -L3*cos(theta) 0;
```

```
                1 0 0 0 0 0 0 L1*sin(alpha)];
            else
                Phiq=[2*(x1-xA) 2*(y1-yA) 0 0 0 0 0 0 ;
                -2*(x2-x1)  -2*(y2-y1)  2*(x2-x1) 2*(y2-y1) 0 0 0 0;
                0 0 2*(x2-xB) 2*(y2-yB) 0 0 0 0;
                0 0 0 0 2*(x3-xB) 2*(y3-yB) 0 0;
                0 0 (x3-xB) (y3-yB) (x2-xB) (y2-yB) 0 0;
                0 0 1 0 0 0 L3*sin(theta) 0;
                1 0 0 0 0 0 0 L1*sin(alpha)];
            end

        end
        %New position
        A=Phiq(:,1:7);
        b=-phi;
        sol=A\b;
        deltaq=[sol;0];
        q=q+deltaq;

x1=q(1);y1=q(2);x2=q(3);y2=q(4);x3=q(5);y3=q(6);theta=q(7);alpha=q(8);
        %Error calculation
        %Condition for sensitivity to variation on angle ALPHA
        if abs(tan(alpha))<1
            %Condition for sensitivity to variation on angle THETA
            if abs(tan(theta))<1
                phi=[(x1-xA)^2+(y1-yA)^2-L1^2;
                (x2-x1)^2+(y2-y1)^2-L2^2;
                (x2-xB)^2+(y2-yB)^2-L3^2;
                (x3-xB)^2+(y3-yB)^2-L4^2;
                (x2-xB)*(x3-xB)+(y2-yB)*(y3-yB)-L3*L4*cos(Lambda);
                (y2-yB)-L3*sin(theta);
                (y1-yA)-L1*sin(alpha)];
            else
                phi=[(x1-xA)^2+(y1-yA)^2-L1^2;
                (x2-x1)^2+(y2-y1)^2-L2^2;
                (x2-xB)^2+(y2-yB)^2-L3^2;
                (x3-xB)^2+(y3-yB)^2-L4^2;
                (x2-xB)*(x3-xB)+(y2-yB)*(y3-yB)-L3*L4*cos(Lambda);
                (x2-xB)-L3*cos(theta);
                (y1-yA)-L1*sin(alpha)];
            end

        else
            %Condition for sensitivity to variation on angle THETA
            if abs(tan(theta))<1
                phi=[(x1-xA)^2+(y1-yA)^2-L1^2;
                (x2-x1)^2+(y2-y1)^2-L2^2;
                (x2-xB)^2+(y2-yB)^2-L3^2;
                (x3-xB)^2+(y3-yB)^2-L4^2;
                (x2-xB)*(x3-xB)+(y2-yB)*(y3-yB)-L3*L4*cos(Lambda);
                (y2-yB)-L3*sin(theta);
                (x1-xA)-L1*cos(alpha)];
            else
                phi=[(x1-xA)^2+(y1-yA)^2-L1^2;
                (x2-x1)^2+(y2-y1)^2-L2^2;
                (x2-xB)^2+(y2-yB)^2-L3^2;
                (x3-xB)^2+(y3-yB)^2-L4^2;
                (x2-xB)*(x3-xB)+(y2-yB)*(y3-yB)-L3*L4*cos(Lambda);
                (x2-xB)-L3*cos(theta);
                (x1-xA)-L1*cos(alpha)];
```

```matlab
        end
    end
    error=norm(phi);
end

%Storing position values for points 1, 2, 3, and angles ALPHA and
THETA
X1(i)=q(1); Y1(i)=q(2);
X2(i)=q(3); Y2(i)=q(4);
X3(i)=q(5); Y3(i)=q(6);
THETA (i)=q(7); ALPHA(i)=q(8);


%Speed PRoblem
bv=-Phiq(:,8)*alphap;
vel=A\bv;

%Storing speed values for points 1, 2, 3, and angle THETA
x1p(i)=vel(1); y1p(i)=vel(2);
x2p(i)=vel(3); y2p(i)=vel(4);
x3p(i)=vel(5); y3p(i)=vel(6);
THETAp(i)=vel(7);


%Acceleration problem
%Condition for sensitivity to variation on angle ALPHA
if abs(tan(alpha))<1
    %Condition for sensitivity to variation on angle THETA
    if abs(tan(theta))<1
        Phiqp=[2*(vel(1)^2+vel(2)^2);
        2*((vel(1)-vel(3))^2+(vel(2)-vel(4))^2);
        2*(vel(3)^2+vel(4)^2);
        2*(vel(5)^2+vel(6)^2);
        2*((vel(3)*vel(5))+(vel(4)*vel(6)));
        L3*vel(7)^2*sin(theta);
        L1*alphap^2*sin(alpha)];
    else
        Phiqp=[2*(vel(1)^2+vel(2)^2);
        2*((vel(1)-vel(3))^2+(vel(2)-vel(4))^2);
        2*(vel(3)^2+vel(4)^2);
        2*(vel(5)^2+vel(6)^2);
        2*((vel(3)*vel(5))+(vel(4)*vel(6)));
        L3*vel(7)^2*cos(theta);
        L1*alphap^2*sin(alpha)];
    end


else
    %Condition for sensitivity to variation on angle THETA
    if abs(tan(theta))<1
        Phiqp=[2*(vel(1)^2+vel(2)^2);
        2*((vel(1)-vel(3))^2+(vel(2)-vel(4))^2);
        2*(vel(3)^2+vel(4)^2);
        2*(vel(5)^2+vel(6)^2);
        2*((vel(3)*vel(5))+(vel(4)*vel(6)));
        L3*vel(7)^2*sin(theta);
        L1*alphap^2*cos(alpha)];
    else
        Phiqp=[2*(vel(1)^2+vel(2)^2);
        2*((vel(1)-vel(3))^2+(vel(2)-vel(4))^2);
```

```
                2*(vel(3)^2+vel(4)^2);
                2*(vel(5)^2+vel(6)^2);
                2*((vel(3)*vel(5))+(vel(4)*vel(6)));
                L3*vel(7)^2*cos(theta);
                L1*alphap^2*cos(alpha)];
        end

    end
    ba=-Phiq(:,8)*a-Phiqp;
    ace=A\ba;

    %Storing acceleration values for points 1, 2, 3, and angle THETA
    x1pp(i)=ace(1); y1pp(i)=ace(2);
    x2pp(i)=ace(3); y2pp(i)=ace(4);
    x3pp(i)=ace(5); y3pp(i)=ace(6);
    THETApp(i)=ace(7);


end

%Position, Speed and Acceleration graphic for point 1
figure('Name','Point 1')
subplot(3,1,1)
plot(ALPHA,X1,'b'); hold on
plot(ALPHA,Y1,'r'); title('Position - Point 1'); xlabel ('Angle
[Rad]');ylabel('Position [mm]');
legend('X','Y')
subplot(3,1,2)
plot(ALPHA,x1p,'b'); hold on
plot(ALPHA,y1p,'r'); title('Speed - Point 1'); xlabel ('Angle
[Rad]');ylabel('Speed [mm/s]');
legend('Vx','Vy')
subplot(3,1,3)
plot(ALPHA,x1pp,'b'); hold on
plot(ALPHA,y1pp,'r'); title('Acceleration - Point 1'); xlabel ('Angle
[Rad]');ylabel('Acceleration [mm/s^2]');
legend('Ax','Ay')


%Position, Speed and Acceleration graphic for point 2
figure('Name','Point 2')
subplot(3,1,1)
plot(ALPHA,X2,'b'); hold on
plot(ALPHA,Y2,'r'); title('Position - Point 2'); xlabel ('Angle
[Rad]');ylabel('Position [mm]');
legend('X','Y')
subplot(3,1,2)
plot(ALPHA,x2p,'b'); hold on
plot(ALPHA,y2p,'r'); title('Speed - Point 2'); xlabel ('Angle
[Rad]');ylabel('Speed [mm/s]');
legend('Vx','Vy')
subplot(3,1,3)
plot(ALPHA,x2pp,'b'); hold on
plot(ALPHA,y2pp,'r'); title('Acceleration - Point 2'); xlabel ('Angle
[Rad]');ylabel('Acceleration [mm/s^2]');
legend('Ax','Ay')


%Position, Speed and Acceleration graphic for point 3
figure('Name','Point 3')
```

```
subplot(3,1,1)
plot(ALPHA,X3,'b'); hold on
plot(ALPHA,Y3,'r'); title('Position - Point 3'); xlabel ('Angle
[Rad]');ylabel('Position [mm]');
legend('X','Y')
subplot(3,1,2)
plot(ALPHA,x3p,'b'); hold on
plot(ALPHA,y3p,'r'); title('Speed - Point 3'); xlabel ('Angle
[Rad]');ylabel('Speed [mm/s]');
legend('Vx','Vy')
subplot(3,1,3)
plot(ALPHA,x3pp,'b'); hold on
plot(ALPHA,y3pp,'r'); title('Acceleration - Point 3'); xlabel ('Angle
[Rad]');ylabel('Acceleration [mm/s^2]');
legend('Ax','Ay')


%Angular Position, Speed and Acceleration graphic for THETA
figure('Name','Angular position - THETA')
subplot(1,1,1)
plot(ALPHA,THETA,'r'); title('Position - \theta'); xlabel ('Angle
\alpha [Rad]');ylabel('Position \theta [rad]');
figure('Name','Angular speed - THETA ')
subplot(1,1,1)
plot(ALPHA,THETAp,'r'); title('Speed - \theta'); xlabel ('Angle \alpha
[Rad]');ylabel('Speed \theta [rad/s]');
figure('Name','Angular acceleration - THETA ')
subplot(1,1,1)
plot(ALPHA,THETApp,'r'); title('Acceleration - \theta'); xlabel ('Angle
\alpha [Rad]');ylabel('Acceleration \theta [rad/s^2]');
```
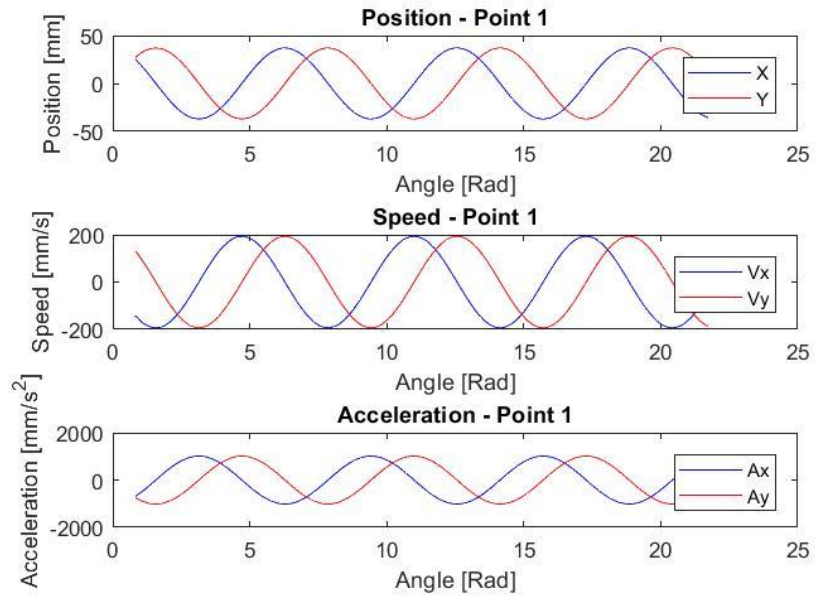
ANNEX II: Kinematic Calculation Results.

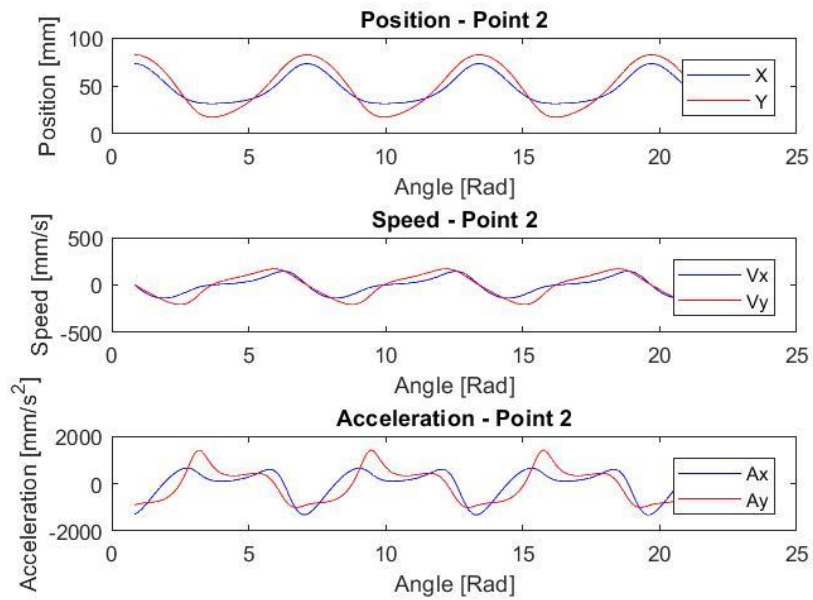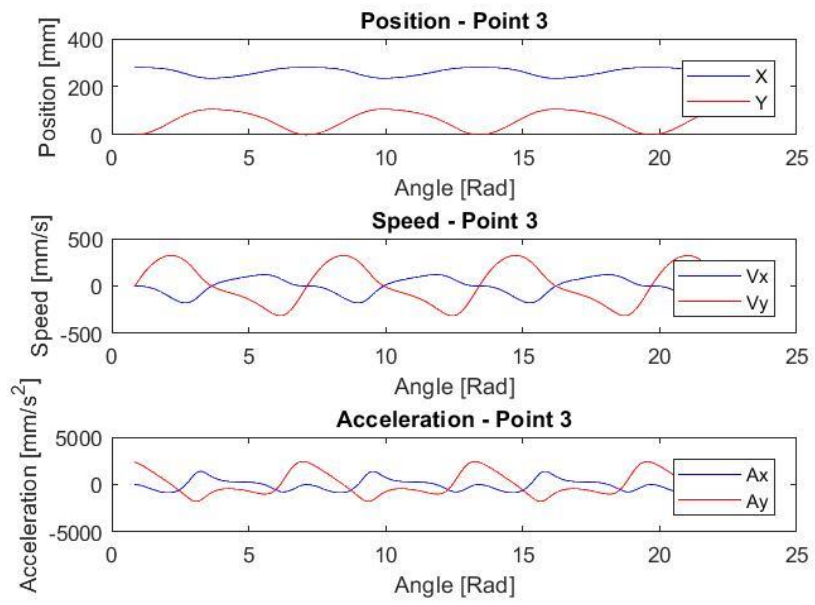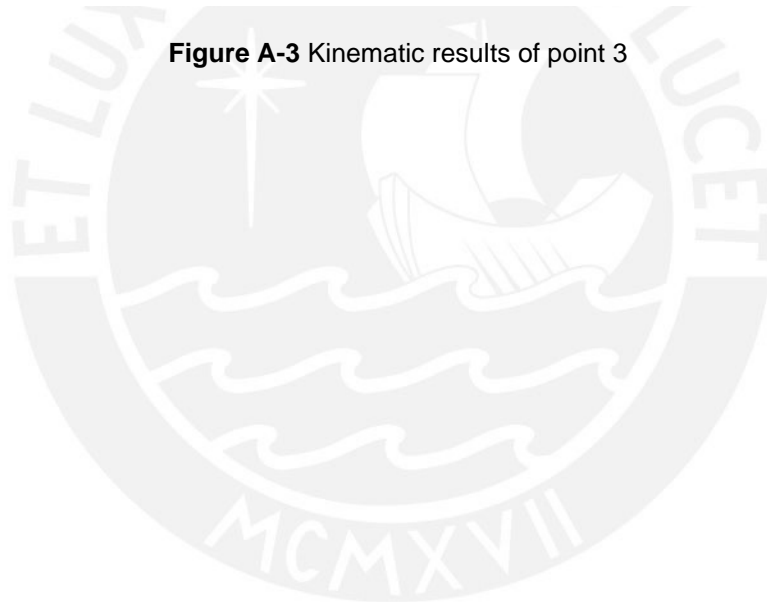**Figure A-1** Kinematic results of point 1

Figure A-2 Kinematic results of point 2

Figure A-3 Kinematic results of point 3

Bibliography

- ALT, Hermann
  1925   "Über die Totlagen des Gelenkvierecks", Zeitschrift für Angewandte Mathematik und Mechanik, Vol 5, pp 337-346.
- ALTROPOL
  2019 a   "NEUKASIL RTV-27 – Data Sheet". Available at: https://www.altropol.de/wp-content/uploads/2019/09/E_RTV_27.pdf
- ALTROPOL
  2019 b   "NEUKASIL RTV-230 – Data Sheet". Available at: https://www.altropol.de/wp-content/uploads/2019/03/E_RTV_230.pdf
- AVELLO, Alejo
  2014   "Teoría de Máquinas", University of Navarra, 2nd Ed., Pp. 130-137
- BAHKTHA Sandesh, Sriharsha HEDGE, Sathish RAO, Nikhil GHANDI
  2018   "Investigation of tensile properties of RTV Silicon based Isotropic Magneto-Rheological Elastomers", MATEC Web of Conferences, 144, 02015.
- BELVIN, Keith, Marco STRAUBEL, W. Keats WILKIE, Martin ZANDER, Juan FERNANDEZ and Martin HILLEBRANDT
  2016   "Advanced Deployable Structural Systems for Small Satellites", Unclassified Document STO-MP-AVT-257, NATO Science and Technology Organization.
- BÖHM, Valter, Philipp SCHORR, Florian SCHALE, Tobias KAUFHOLD, Lena ZENTNER and Klaus ZIMMERMANN
  2021   "Worm-Like Mobile Robot Based on a Tensegrity Structure", 4th International Conference on Soft Robotics, Pp, 358-363.
- CHAVEZ, Jhohan, Philipp SCHORR, Tobias KAUFHOLD, Lena ZENTNER, Klaus ZIMMERMANN and Valter BÖHM
  2020   "Influence of Elastomeric Tensioned Members on the Characteristics of Compliant Tensegrity Structures in Soft Robotic Applications", 5th International Conference on System-Integrated Intelligence, Pp. 289-294.
- CHAVEZ, Jhohan, Marek ZIOLKOWSKI, Philipp SCHORR, Lothar SPIEß, Valter BÖHM and Klaus ZIMMERMANN
  2021   "A Method to Aproach Constant Isotropic Permeabilities and Demagnetizations Factors of Magneto-Rheological Elastomers", Journal of Magnetism and Magnetic Materials 527, 167742.
- ENCICLOPEDIA BRITANNICA
  2022   "Taylor Series", March 10th 2022 [Online], Available at: https://www.britannica.com/science/Taylor-series [Accesed 2022]
- FULLER, Richard
  1959   "Tensile-Integrity Structures" (U.S. Patent Nº 3'063,521), United States Patent Office.

- FURUYA, Hiroshi
  1992   "Concept of Deployable Tensegrity Structures in Space Application", International Journal of Space Structures, Vol. 7, No. 2, Pp. 143-151.
- HEARTNEY, Eleanor and Kenneth SNELSON
  2013   "Kenneth Snelson, Art and Ideas", New York: Marlborough Gallery.
- KAUPO
  2016   "Ecoflex series – Data sheet". Available at:
             https://www.kaupo.de/shop/out/media/ECOFLEX_SERIE.pdf
- KOCH, Jeremy, Daniel CASTANEDA, Randy EWOLDT and David LANGE
  2019   "Vibration of fresh concrete understood through the paradigm of granular physics", Cement and Concrete Research, Vol. 115, Pp. 31-42.
- LEVIN, Stephen
  1982   "Continuous Tension, Discontinuous Compression: A Model for Biomechanical Support of the Body", Bulletin for Structural Integration, Vol. 8, No. 1, Pp. 31-33.
- LOPEZ, Alexander
  2019   "Investigations and simulations of magneto elastomer materials (MSE) influenced by static magnetic fields for soft robotics applications".
- LUCK Kurt and Karl-Heinz MODLER
  1995   "Getriebetechinik, Analyse, Synthese, Optimierung". Springer, 2nd Ed. Pp. 192-195.
- MARX, Uwe
  1994   "Die Übertragunswinkel in ebene Mechanismen", Mechanism and Machine Theory, Vol. 29, Pp. 907-915.
- MENESES, Jesus
  2019a   "Coordenadas en Mecanismos – Apuntes de Clase", PUCP,
- MENESES, Jesus
  2019b   "Modelación Cinemática de Mecanismos – Apuntes de Clase", PUCP.
- PUGA, Helder, Joaquim BARBOSA, Vitor Hugo CARNEIRO, Flavia BARBOSA, Jose Carlos TEIXEIRA
  2021   "Optimizing high-volume ultrasonic melt degassing using synchronized kinematic translation", Journal of Materials Research and Technology, Vol 14, Pp. 2832-2844.
- SCHORR Philipp, Florian SCHALE, Jan Marc OTTERBACH, Lena ZENTNER, Klaus ZIMMERMANN and Valter BÖHM
  2020   "Investigation of a Multistable Tensegrity Robot Applied as Tilting Locomotion System", IEEE International Conference on Robotics and Automation.
- SORIA, Cintya, Luis PALACIOS, Alexis ELIAS, Imperio PERALES and Oscar MARTINEZ
  2019   "Investigation of the Effect of Carbonyl Iron Micro-Particles on the Mechanical and Rheological Properties of Isotropic and Anisotropic

MREs: Constructive Magneto-Mechanical Material Model", Polymers, 11, 1705.

- SUMI, Susanne, Valter BÖHM and Klaus ZIMMERMANN
  2017   "A Multistable Tensegrity Structure with a Griper Application", Mechanism and Machine Theory 114, Pp. 204-217.

- SWANSON, Randel
  2013   "Biotensegrity: A Unifying Theory of Biological Architecture with Applications to Osteopathic Practice, Education and Research – A Review and Analysis", The Journal of the American Osteopathic Association, Vol. 113, No. 1, Pp. 34-52.

- TU-ILMENAU
  2020 a   "Soft Tensegrity Structures with Variable Stiffness and Shape Changing Ability", Fachgebiet Mechanik Technik.

- TU-ILMENAU
  2020 b   "Vorlesungs und Übungsmaterial zum Lehrfach Getriebetechnik 2", Fachgebiet Nachgiebige Systeme

- WANG, Hui, Zhenyan CHEN, Youming CHEN, Mingjie XIE and Lin HUA
  2019   "Mechanism study of bubble removal in narrow viscous fluid by using ultrasonic vibration", Japanese Journal of Applied Physics, Vol. 58, 115503.